Transparent Conducting Electrodes for Perovskite-Silicon Tandem Solar Cells

John O'Sullivan[a], Matthew Wright[a], Bruno Vicari Stefani[b], Paul Llontop[c], Abderrahime Sekkat[d,e], Robert L. Z. Hoye[e], Monica Morales-Masis[c], Ruy S. Bonilla*[,a]

[a] Department of Materials, University of Oxford, Oxford, OX1 3PH, United Kingdom

[b] CSIRO Energy, Newcastle Energy Centre, 10 Murray Dwyer Circuit, Mayfield West, NSW 2304, Australia

[c] MESA+ Institute for Nanotechnology, University of Twente, Enschede 7500 AE, The Netherlands

[d] Univ. Toulouse, CNRS, Toulouse INP, LGC, Toulouse, France.

[e] Inorganic Chemistry Laboratory, University of Oxford, Oxford, UK

*Corresponding author e-mail: sebastian.bonilla@materials.ox.ac.uk

Abstract – Transparent conducting electrodes (TCEs) combine high optical transmittance and electrical conductivity, and are an essential component of optoelectronic devices, such as solar cells. A major recent advance in photovoltaic (PV) technology is the integration of industry-dominant crystalline silicon solar cells with metal-halide perovskite absorbers that harvest a complementary part of the solar spectrum. These perovskite-silicon tandem cells offer a pathway to power conversion efficiencies (PCEs) exceeding 40% at low cost, but introduce new challenges for TCE design. In tandem cells, TCEs serve multiple roles: enabling lateral charge transport as well as facilitating interface charge collection or recombination, all while minimising parasitic absorption or reflection across a broad wavelength range. TCEs must also remain compatible with diverse materials and delicate fabrication processes. Achieving this balance of optical, electrical, and chemical properties has so far limited practical TCEs in tandems to a small set of high-cost, indium-based oxides. Recent advances in computational and experimental techniques have improved understanding of TCE solid-state physics, revealing promising alternative materials. In this review, we examine the material properties essential for TCEs in perovskite–silicon tandems, evaluate current candidates, and highlight the key challenges and opportunities for next-generation TCE development. Our goal is to bridge the gap between materials science and device engineering, providing a roadmap to accelerate the integration of advanced TCEs in high-efficiency optoelectronic devices.

1 Introduction

Single-junction crystalline silicon (c-Si) solar cells are approaching their theoretical power conversion efficiency (PCE) limit of 29.4%[1,2], or up to 30.1% with single-axis tracking[3], with LONGi Solar recently reporting a certified PCE of 27.81% for a silicon heterojunction (SHJ) hybrid back-contact cell[4,5]. A major limit to the single-junction PCE is charge-carrier thermalisation, where carriers generated through the absorption of photons with energy above the absorber bandgap lose excess energy as heat. Tandem solar cells reduce such losses by combining multiple absorbers with differing bandgaps, each converting a complementary fraction of the spectrum into electricity. While III-V tandems can reach 47.6% PCE under 600-sun concentration, they remain too expensive for mass-production[6]. This can be mitigated by exploiting lead-halide perovskite absorbers, hereafter "perovskites". Their ABX_3 stoichiometry enables bandgap tuning through compositional variations that can be exploited to complement silicon absorbers, increasing PCE, and reducing the levelised cost of electricity of PV[7–11]. In perovskite-silicon tandems, a low-bandgap silicon cell (1.12 eV) is positioned beneath a wide-bandgap perovskite cell (~1.6 to 1.8 eV). High-energy photons are absorbed by the perovskite, while lower-energy photons pass through to be absorbed by silicon. Lab-scale (1 cm^2) perovskite-silicon tandem PCEs have risen from <14% in 2015, to 34.85% in 2025[12,13], though this is far from their ~45% theoretical maximum under AM1.5G illumination[13–17]. Transparent conducting electrodes (TCE) are a major source of loss, but are required for light transmission and lateral charge transport. TCEs also interconnect sub-cells, enabling voltage addition. TCEs contribute resistive, absorptive, and reflective losses, reducing PCE by >2% in absolute terms ($\%_{abs}$) per TCE used[7,18–25]. In tandems, each absorber is interconnected by an additional TCE, compounding losses[26,27]. Commercial TCEs, such as tin-doped indium oxide (ITO), long used in solar cells, touchscreens and organic light-emitting diodes, introduce significant losses in tandems. Improved understanding of TCE physics in tandem devices is essential to realise PCEs >40%.

The optimum trade-off between sheet resistance (R_{sheet}) and transmittance (T_x) is often expressed as a TCE's "figure of merit" (FoM)[24,28–32]. However, the differing requirements in tandems render simple two-parameter metrics insufficient. Fig. 1a depicts TCE placement in two-terminal (2T) and four-terminal (4T) tandems. 2T cells require 2-3 TCEs, while 4T cells may require four TCEs and an optical spacer between sub-cells. In 4T modules, additional wiring for sub-cell connection to inverters increases the power-electronics, assembly, and cabling costs, and their need for additional and thicker TCEs increases parasitic absorption[33–35]. 2T cells are therefore the most promising for low-cost scalable manufacturing, and so will be the focus of this review.

Fig. 1b summarises TCE-related resistive and optical losses in 2T tandems. Front-TCEs require low R_{sheet} for efficient lateral charge transport to metal fingers (low R_L), and high broadband transmittance (requiring low absorptance A_x and low reflectance R_x) to maximise absorption in both absorbers[19,36,37]. The mid-TCE requires higher lateral resistances ~200-1000 Ω/□ to prevent shunting, and high transmittance >500 nm. The rear-TCE is electrically similar to the front, but must reflect photons back into the silicon while minimising plasmonic losses[38,39]. In some architectures, the rear-TCE is replaced by a highly-doped silicon layer, typically referred to as an emitter or back-surface field[40]. Fig. 1c depicts TCE absorptance overlaid on perovskite and silicon external quantum efficiency, highlighting the near-UV (<450 nm) and the near-IR (900-1200 nm) as primary loss regions. The varying requirements across sub-cells render any single FoM inadequate, as TCE target properties depend on adjacent layers, architecture, and position.

TCEs must have low transfer and contact resistance (R_t, R_c) and minimise interfacial non-radiative, Shockley-Read-Hall (SRH) recombination[41–45]. Their refractive indices must match adjacent layers to minimise reflection[19]. Processing requires that TCEs be deposited without

compromising adjacent-layer stability[46–48], and remain stable under long-term operation[19,49,50]. TCEs may also need to block ion migration and solvent permeation[51–53]. Finally, TCEs must be fabricable rapidly, at low cost, over large, often textured areas[53]. Few materials meet all these demands.

Existing TCEs used in tandems include transparent conducting oxides (TCOs), metal nanowires[15], and ultrathin metals. Fig. 1d presents front-TCE usage in 2T perovskite-silicon tandems reported since 2015, highlighting reliance on zinc-doped indium oxide (IZO), ITO, and other doped indium oxides. But indium scarcity constrains the manufacturing capacity of such devices to <200 GW/y, well below the 3-4 TW/yr required to meet 2050 climate targets[7,9,11,20,54–56]. Indium-based TCEs are also undesirable due to their high cost, and can comprise >50% of the cost of perovskite cells[57]. Indium reduction strategies include modifying sputtering targets[58] and multilayer TCEs[59–63], but indium-free tandem cells are yet to achieve >20% PCE[64]. Novel TCE development is therefore essential.

Recent advances in density functional theory (DFT) have revealed novel TCE mechanisms such as resonant doping[65,66] and polaronic conduction[67,68]. Simulations indicate that plasmonic metamaterials and nanophotonics can improve TCE optical coupling[69–75]. Additionally, 2D materials such as MXenes, transition-metal dichalcogenides, and graphene may improve passivation, stability, and charge-carrier extraction[76–79]. Yet, these remain underutilised in practical devices, where research has focused on improving perovskite stability and passivation, texturing, and enhancing charge-carrier extraction using self-assembled monolayers (SAMs)[8,38,53,80,81]. As tandems approach their limits using conventional TCEs, progress will depend on the convergence of materials physics and device engineering to develop sustainable, high-performance TCEs.

Several excellent reviews have surveyed TCE physics in isolation[19,75,82–85]. Here, we emphasise that TCEs cannot be understood independently of the tandem cell architecture. Interfacial effects, competing scattering mechanisms, plasmon resonances and band transitions, must be considered alongside processing and operation constraints. Section 2, overviews TCE material classes and the mechanisms governing their optoelectronic properties. Sections 3 and 4 examine how interfaces dictate TCE functionality in tandems, from charge transport to optical coupling. We then review TCE properties for practical integration in devices, and how these evolve when transferring from lab to industrial scales. Finally, we discuss strategies to develop sustainable high-performance TCEs. We aim to guide physicists, materials scientists, and engineers in benchmarking TCE properties in the context of tandem solar cells. This understanding will be key in developing high-performance, scalable, perovskite-silicon tandem devices with PCE >40%, delineating pathways to reach >50% in multi-junction cells[21], and unlocking the full potential of TCEs for next-generation devices beyond PV.

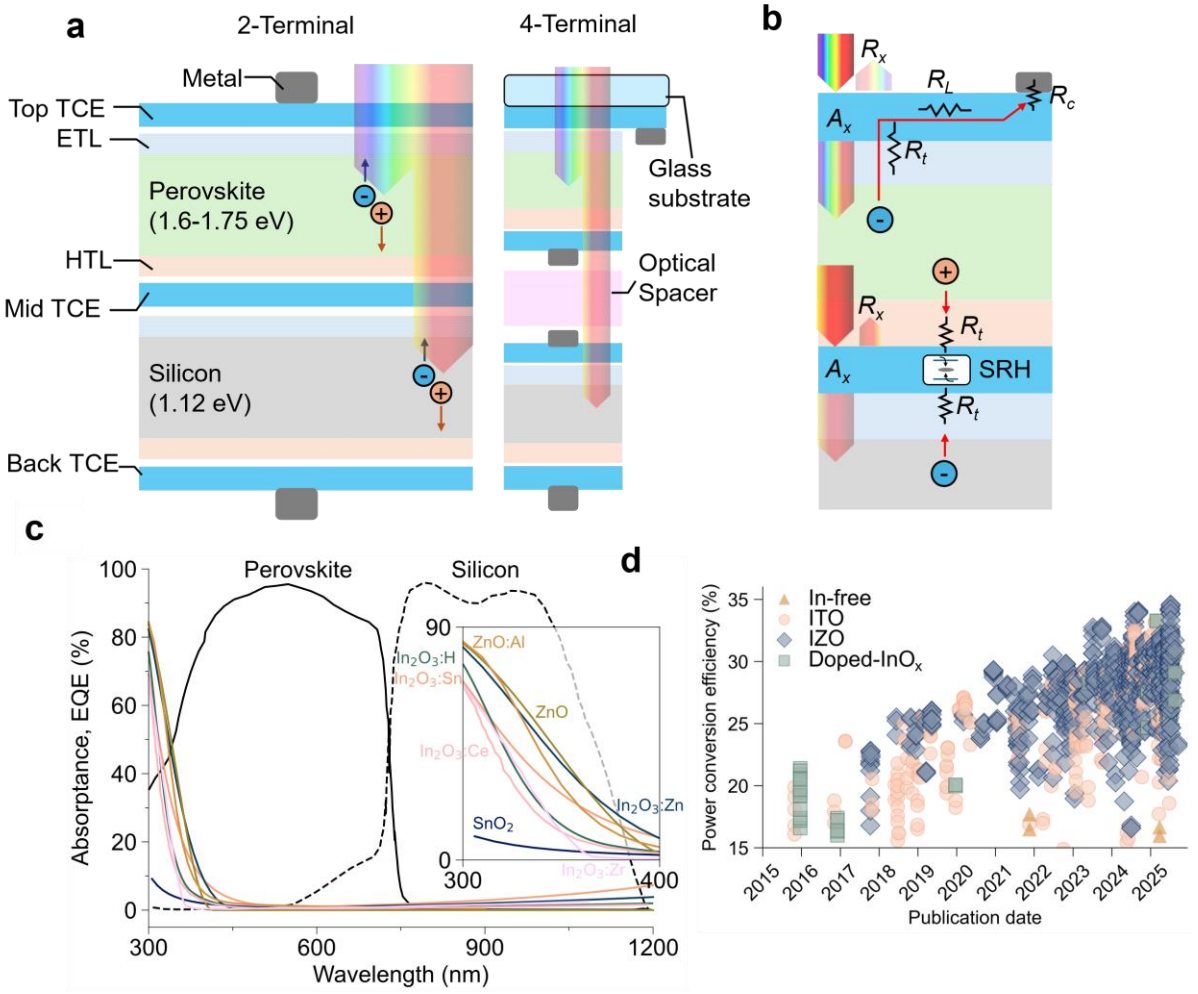

Fig. 1: Transparent conducting electrodes in perovskite-silicon tandem solar cells: TCE Role, optical response, and power conversion efficiency. a. TCEs in perovskite-silicon tandem solar cells in 2T and 4T configuration. **b**. The role of TCEs in charge collection and transport, including losses originating from absorption (A_x), reflection (R_x), carrier transfer resistance (R_t), lateral resistance and carrier scattering (R_L), metal contact resistance (R_C), and Shockley-Read Hall (SRH) recombination. **c**. TCE absorptance (%) (coloured lines) with respect to wavelength overlaid with perovskite and silicon external quantum efficiency (EQE) with respect to wavelength. **d**. Review of front-TCEs in 2T perovskite-silicon tandem solar cells reported from January 2015 to August 2025. ITO and IZO refer to tin-doped indium oxide and zinc-doped indium oxide respectively. Doped-InO_x refers to indium oxide doped with other elements: Ce, Zr, W, or H. The data used to plot **c**. and **d**. can be found in the Supplementary Information, Tables S3, S7 and S8, with data for perovskite and silicon EQE **c**. extracted from ref.[86].

Box 1: Fundamental properties of TCEs

The resistivity of a uniformly doped material is $\rho = 1/(q \cdot N \cdot \mu)$, where *q, N,* and *μ* are the majority-carrier charge (Coulombs), concentration (cm^{-3}), and mobility (cm^2/Vs)[85,87,88]. The sheet resistance is $R_{sheet} = \rho/t$, where *t* is thickness. Mobility can be defined as $\mu = q\tau/m^*$, where τ is the carrier relaxation time, indicating the average time between two scattering events, and *m** is the carrier effective mass[89]. Mobility therefore increases when scattering sources are reduced, *and m** is minimised[85]. Increasing carrier concentration can reduce mobility via impurity scattering following Conwell-Weisskopf theory, so requires careful control[19,85,90,91].

Transmittance (T_x) follows the Beer-Lambert law: $T_x(\lambda) = (1 - R_x(\lambda))^2 \cdot e^{-\alpha(\lambda)\cdot t}$, where R_x is reflectance, and *α* is the absorption coefficient[83,87]. Increasing t reduces R_{sheet}, but also T_x, thus these properties must be balanced. Increasing *N* can lower R_{sheet}, but reduces T_x through free carrier absorption (FCA), following the Drude model of *α*[19,83,92]:

$$\alpha = \frac{\lambda^2 q^3 N}{4\pi^2 \varepsilon_0 c^3 n (m^*)^2 \mu_{opt}}, (1)$$

where *λ* is wavelength, ε_0 is the permittivity of free space, *c* the speed of light in vacuum, n the refractive index, and μ_{opt} the optical mobility (mobility not inclusive of grain-to-grain scattering). The wavelengths absorbed depend on the natural frequency of oscillation of the free electron gas, described by the plasma wavelength λ_p[93]:

$$\lambda_p = 2\pi c \sqrt{\frac{m^* \varepsilon_{TCE}}{N q^2}}, (2)$$

For incident light $\lambda < \lambda_p$, the real part of the dielectric function is positive, and the material behaves as a dielectric: free electrons cannot respond fast enough to the oscillating electromagnetic field, and light passes through. For $\lambda > \lambda_p$, the real part of the dielectric function becomes negative, and the TCE reflects or absorbs incident radiation[92,93]. For most TCEs, λ_p is in the near-IR: while visible and UV light pass through, near-IR and IR light is lost[94–98]. TCE materials with high λ_p are therefore necessary. This is achieved by reducing *N,* and increasing *m**, *μ* and ε_{TCE}. As a high *m** increases *α*, it is preferable to develop TCEs with high *μ* and ε_{TCE}.

The most common TCEs are *n*-type TCOs. These are oxides of post-transition metals in $(n-1)d^{10}ns^2np^0$ configuration[99,100]. Metal (M) *s*-orbital and the oxygen *p*-orbital interactions generate a bandgap >3 eV. The conduction band (CB) is formed by antibonding M *s*–O *p* states, while the valence band (VB) is formed by bonding and nonbonding states with primarily O 2*p* character[19,99]. In *n*-type TCOs, *m** is determined by the curvature of the CB, where high dispersion leads to low *m**[89]. Conductivity is achieved by degenerately doping TOCs beyond the Mott criterion, increasing their Fermi energy (E_F) into the CB or VB[85,101,102], and widening the optical bandgap via the Burnstein-Moss effect[85]. The dopants perturb the CB and increase *m**, therefore shallow dopants which minimally disturb and do not hybridise with the CB are preferred. An electron affinity (E_A) of >4 eV typically desired to more easily dope degeneratively[68,85,103]. Doping density should be controlled, as increasing doping reduces the work function (Φ_{TCE}), and increases scattering.

2 Material families and their optoelectronic properties

While there are many TCE materials, the most common are *n*-type metal oxides, referred to as *n*-type TCOs. These wide-bandgap semiconductors are doped to introduce excess electrons via lattice defects such as oxygen vacancies or substitutional impurities, which create states near the conduction band (CB) minimum, E_c[85,104]. Fig. 2a illustrates the Fermi level shifting above E_c through *n*-type doping to achieve degeneracy[105]. TCOs based on In_2O_3,

ZnO and SnO_2 are commonly used due to their wide bandgaps (3.37–4.3 eV)[106–108], which suppress visible interband transitions and thus optical absorption[109]. Their highly-dispersive conduction bands (CBs) minimise effective mass (m^* from 0.18-0.28m_0)[110–115]. Though intrinsically insulating, doping enhances conductivity and transparency via increased carrier concentration and the Burstein–Moss effect[98]. Beyond carrier addition, dopants hybridise with the metal *n*s states forming the host CB. Dopant orbital symmetry strongly influences CB dispersion: *s* and *p*-orbital dopants (e.g., $Sn^{4+}\rightarrow In^{3+}$ in In_2O_3[82,116], $Al^{3+}\rightarrow Zn^{2+}$ in ZnO[106], $F^-\rightarrow O^{2-}$ in SnO_2[117]) introduce shallow donors that hybridise efficiently with the host metal *ns* orbitals. This hybridisation modifies the density of states and enhances CB delocalisation. Shallow donors thus preserve the CB dispersion and low electron effective mass (m^*), enabling high electron mobility[82,118,119]. Hydrogen can also introduce shallow donors, although often with poor stability[120–122]. Certain *d*-orbital dopants such as $Mo^{6+}\rightarrow In^{3+}$ in In_2O_3, form resonant donor states that minimally perturb the CB, preserving low m^*, and high mobility >100 cm^2/Vs[66].

Minimising ionic-radius mismatch between host and dopant reduces lattice distortion and defect scattering, improving mobility[123,124]. The low resistivity of ITO (<10^{-3} Ω cm) partly arises from the close match between Sn^{4+} (0.69 Å) and In^{3+} (0.80 Å) radii[125]. This enables efficient substitution with minimal lattice strain, and promotes oxygen vacancies formation, resulting in carrier concentrations ~10^{20}-10^{21} cm^{-3} [119,126,127]. In IZO, Zn^{2+} (0.74 Å) similarly matches In^{3+}, reducing scattering. Amorphous IZO dominates as the front-TCE in perovskite-silicon tandems due to its high mobility at low deposition temperatures, and low FCA, although its blue-region absorption remains high owing to its diffuse band edge[128–130], motivating the search for alternative dopants. Zr^{4+} and Ce^{4+} doped In_2O_3 have been recently demonstrated in tandems, showing high mobilities >70 cm^2/Vs, reflecting their ionic radii of 0.86 Å and 0.87 Å respectively[44,89,131,132].

Aluminium-doped ZnO (AZO) and gallium-doped ZnO (GZO) are attractive for their low-cost and sustainability[133]. However, their lower mobilities (~5-15 cm^2/Vs for AZO, ~9-30 cm^2/Vs for GZO) limit conductivity[133–137]. Their low mobility arises from their polycrystallinity, causing high grain-boundary scattering, exacerbated by defects and trapping. This scattering is dependent on grain size, orientation, doping, and deposition conditions[138,139]. These TCOs also have poor damp-heat stability, as their numerous grain boundaries act as reactive sites and diffusion pathways for moisture and oxygen. Under 1000 h at 90% relative humidity, resistivity can increase by 3.5× due to accelerated defect formation[140–144]. Grain boundaries can also facilitate deleterious metal-ion migration, e.g. copper[145]. ZnO-based TCEs may also chemically react with perovskites due to their basicity, necessitating buffer layers to prevent perovskite decomposition[146]. These factors have limited the long-term reliability and adoption of AZO and GZO.

TCE fabrication methods determine film microstructure (see Boxes 2 and 3) and whether films are amorphous or polycrystalline. Effective mass, however, remains a fundamental constraint on conductivity. Evaluating TCOs requires distinguishing such intrinsic factors (band dispersion, m^*, ionic-radius mismatch) that set the mobility limit, from extrinsic factors (crystallisation, device integration, grain boundary scattering) that can be improved. For optical comparison, absorption coefficient should be used, as interference effects, such as Fabry–Pérot oscillations, depend on thickness and can distort transmittance measurements[147]. The absorption coefficient reflects the intrinsic optical material response, enabling thickness-independent comparison. Fig. 2b illustrates the weighted-average absorption coefficient of different TCOs in the 300-750 nm (perovskite) and 750-1200 nm (silicon) regions. Undoped ZnO, SnO_2 and In_2O_3, exhibit low absorptance, but doping is required to achieve adequate conductivity. When doped, AZO and FTO show high IR absorptance, largely driven by high FCA, making integration challenging without imparting significant losses. By contrast, In_2O_3 can largely maintain or even reduce absorptance using certain dopants. The excellent performance of IZO, IZrO and ICO as front-TCEs is a direct consequence of their low

weighted-absorption coefficient across both spectral regions. But optical and electrical properties must be balanced. Fig. 2c compares the carrier concentration and mobility of various TCOs at different fabrication temperatures. The dominance of doped-In_2O_3 TCOs is clear from their clustering in the high-mobility, high carrier concentration region. This combination is inaccessible for ZnO or SnO_2-based alternatives due to challenges in stable doping without substantial CB perturbation and scattering. Achieving high-performance ZnO and SnO_2-based TCOs requires methods to incorporate dopants that promote high mobility.

Beyond TCOs, graphene, metal nanowires (NWs), and ultrathin metals have been used in tandems[148]. Graphene offers high transmittance (>95%), and is an effective ion/moisture barrier[149], but suffers from high R_{sheet} (~300 Ω/□) and work function mismatching with perovskite charge transport layers (CTLs)[149,150]. Metal NWs provide low R_{sheet} (~0.01–10 Ω/□) and flexibility but face adhesion, stability, and surface roughness limitations[151–153]. Ultrathin metals offer low-temperature processing, and are often used as interconnect TCEs in all-perovskite tandems[53,79,81,154–157]. However, ultrathin films are difficult to fabricate due to their low surface energy[158,159], and they can be unstable to oxygen, moisture, heat, and ion migration[157,160]. Despite multilayer dielectrics and seed layers improving growth, ultrathin metals remain ultimately too absorptive to compete with TCOs in tandems[158].

These alternative materials for included for completeness but represent a small proportion of TCEs used in reported tandem cells as they cannot yet match TCOs in terms of mobility, transmittance, processing compatibility, and scalability. These limitations may be overcome by combining nanomaterials with metal oxides to form hybrid nanocomposites. For example, metal NWs coated with thin metal oxide layers to improve stability and band alignment[161,162]. These materials have not yet been implemented in tandems, but may become viable if scalable fabrication yields high mobility and processing compatibility with adjacent layers. For the foreseeable future, TCOs are expected to remain the dominant TCEs used in tandems. In the following two sections, we discuss how these materials interface with adjacent layers, focusing on improving electrical and optical transport.

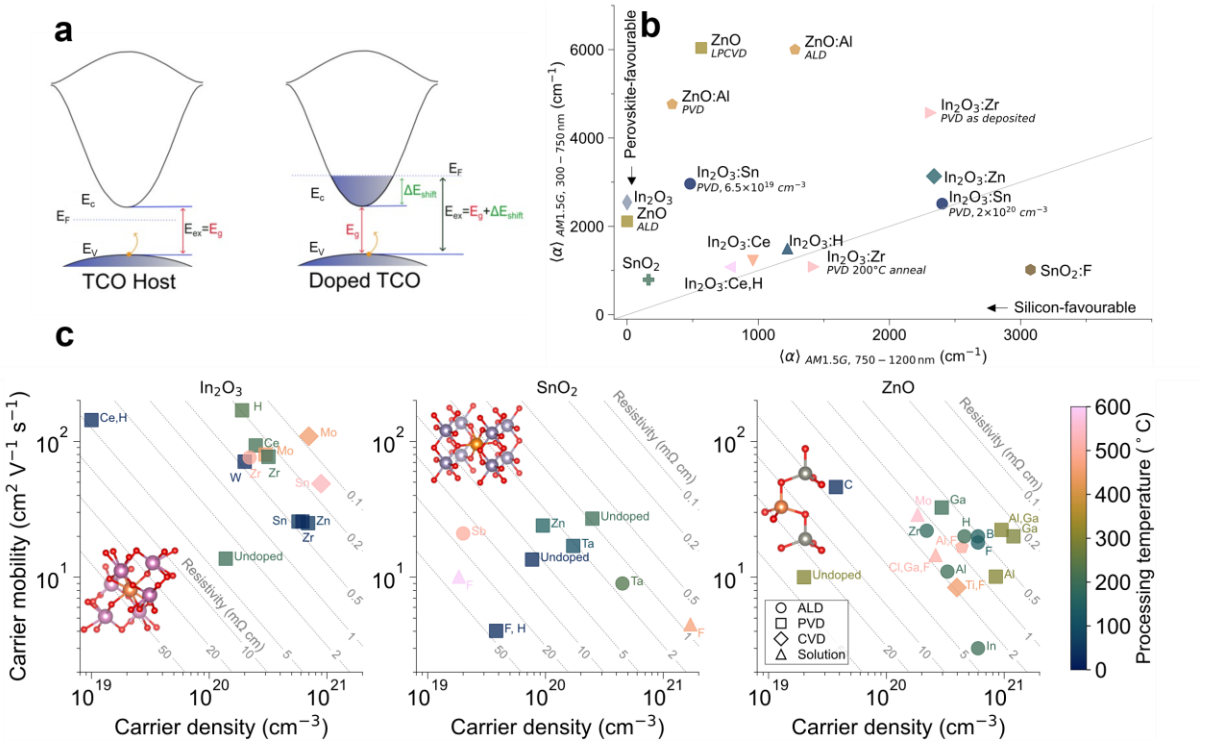

Fig. 2: Effect of doping on the material properties of wide bandgap transparent conducting oxides. a. Schematic of the band structure of a transparent metal-oxide with wide bandgap (E_g) without (left) and with (right) degenerate doping. In the latter, the Fermi level has shifted into the conduction band by an energy ΔE_{shift}, via the "Burnstein-Moss Shift", enabling conduction. E_c and E_v refer to conduction and valence band edges, respectively. Figure design adapted from Fig. 1, ref.[105]. **b**. Weighted-average absorptance <α> of TCOs to the AM 1.5 spectrum, separated into regions 300-750 nm and 750-1200 nm, with several deposition techniques compared: low-pressure chemical vapour deposition (LP-CVD), atomic layer deposition (ALD), and physical vapour deposition (PVD). **c**. Carrier mobility vs carrier density of a range of TCOs. The diagonal lines correspond to bulk resistivity in mΩ cm. Ball and stick models of the crystal structure of the wide bandgap oxide are given in the inset. The data used to plot **b**. and **c**. can be found in the Supplementary Information, Tables S5, and S7 and S8.

Box 2: Manufacturing and Processing

In tandem solar cells, TCEs must be compatible with thermally-sensitive device layers. Monolithic designs require low-temperature, low-damage deposition to avoid degrading the perovskite absorber or charge transport layers. This limits TCE deposition to <110 °C for perovskites (composition dependent)[34], and <200 °C for a-Si[163]. In contrast, four-terminal tandems allow high-temperature TCE deposition on the glass side of the perovskite top cell, enabling improved TCE crystallisation.

TCE fabrication methods fall into three approaches: Physical Vapor Deposition (PVD), Chemical Vapor Deposition (CVD), and solution processing. Each presents trade-offs in thermal budget, film quality, and substrate damage—key factors that impact device power conversion efficiency and stability. The panel below schematically summarises the main deposition techniques, with spider plots comparing their attributes. The methodology and assumptions behind this comparison are given in Supplementary Information, Section S.4.

Physical Vapour Deposition (PVD) uses vacuum-based systems and high-purity metal or metal-oxide targets. Vaporisation sources include direct current (DC) or radio frequency (RF) sputtering, ion beam or electron beam deposition/evaporation (IBD, EBE), and rapid

plasma or pulsed-laser deposition (RPD, PLD) techniques. Vaporised species react with background oxygen to form TCO films, with properties tuned by working pressure and temperature. However, sputtering can produce highly energetic particles and plasma that damage underlying layers[164]. Mitigation strategies include using buffer layers such as ALD SnO_2 or evaporated MoO_x, and alternative deposition designs[46]. Low power "soft" sputtering can reduce damage but lowers mobility due to insufficient crystallisation energy. There is therefore a trade-off between damage and film quality. We refer readers to detailed reviews of PVD TCO deposition for PV where these processes are discussed comprehensively[46,165].

Chemical Vapour Deposition (CVD) introduces organometallic and oxidant gases (e.g. O_2, O_3 or H_2O) into a reactor to promote film formation via surface reactions on heated substrates. Variants include atmospheric and low-pressure CVD (APCVD, LPCVD), plasma-enhanced CVD (PECVD), aerosol-assisted CVD (AACVD) and hot-wire CVD (HWCVD). Atomic layer deposition (ALD), a subset of CVD, allows atomic-scale control through alternate precursor dosing and purging. Spatial ALD further enhances throughput and manufacturing flexibility. CVD methods are generally gentler on substrates than PVD but often require uniform -OH termination for uniform nucleation and film growth[166], and can involve reactive precursors that may induce unwanted surface reactions[167,168]. A key benefit of ALD-based deposition is its ability to provide highly conformal coatings on textured, high-aspect ratio structures[167,169,170]. This enables thinner, pinhole-free layers with reduced absorptance and improved interfacial contact, such as on textured silicon[171,172], or for coating metal nanowires with TCOs to improve stability[170].

Solution processing uses precursor salts or suspended metal oxide nanoparticles in solvent, deposited via spin coating, spray coating, or screen-printing. Annealing then promotes solvent evaporation and TCO formation. The final microstructure and stoichiometry are largely defined by the post-deposition thermal treatment. While generally rapid and low-cost, there is limited thickness control, and typically low mobility.

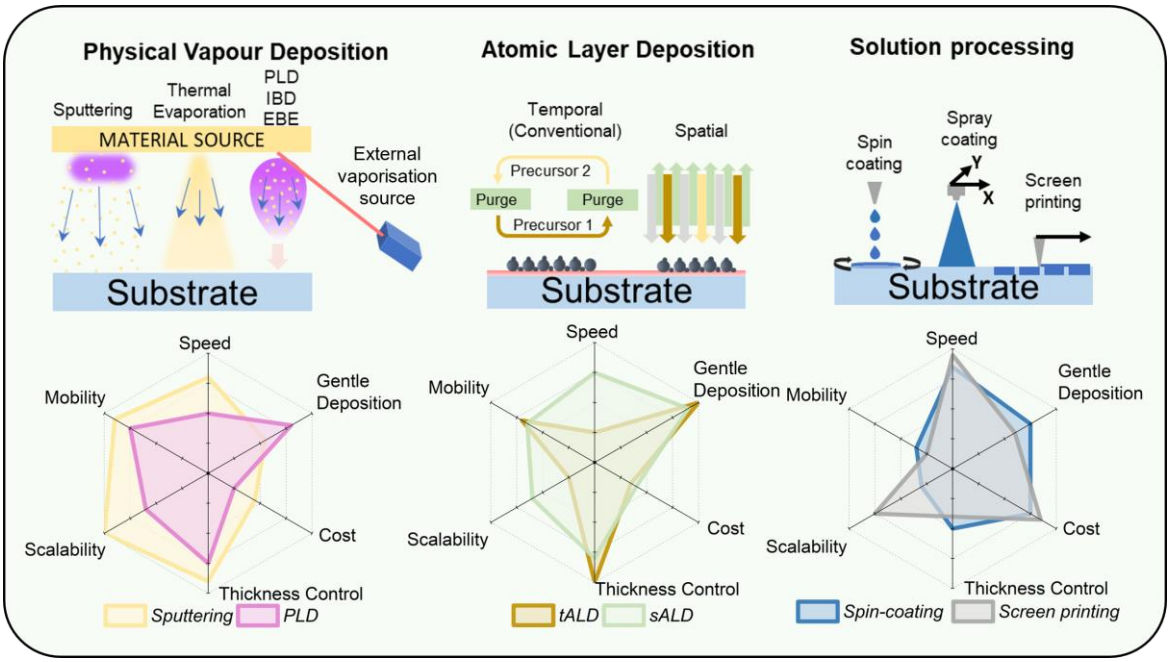

236

3 Electronic Band Structure and Interface Charge Transport

Fig. 3a depicts the electronic band diagram of a typical 2T tandem, comprising a p-i-n-perovskite device on a SHJ cell. The diagram highlights vertical transport mechanisms and the junctions and interfaces that create barriers to energy flow. At each junction, different charge-transport mechanisms operate. Energy barriers at junctions reduce charge-carrier transport and increase the potential energies for extraction, causing voltage losses. Here we discuss these transport mechanisms, targeting how TCE band structure influences carrier extraction[45,173].

3.1 Charge Collection from Perovskite Absorbers

After an electron-hole pair is photo-generated in the perovskite, carriers flow through the absorber: electrons toward the electron transport layer (ETL), and holes toward the hole transport layer (HTL). The energy barrier between these materials (ΔE), or band offset (BO), determines the transport mechanism, and interface voltage loss. For lossless "band transport" (BT), the TCE work function (Φ_{TCE}) must align to the conduction or valence band edges (E_c, E_v) of the ETL or HTL, respectively. At the electron-transport side, the conduction band offset (CBO) should be slightly negative to promote electron extraction, while a large valence band offset (VBO) blocks hole injection. Conversely, at the hole-transport side, the TCE work function Φ_{TCE} must be close to, but slightly positive compared to the HTL valence band edge (E_V), to promote hole transport, with large conduction band offset (CBO) to block electrons.

If the energy barrier (ΔE) between TCE and ETL/HTL is $\gtrapprox$0.3 eV, alternative transport mechanisms such as thermionic emission (TE) or trap-assisted-tunnelling (TAT) may be required. These processes are relatively lossy compared to band transport, contributing to thermalisation and recombination losses. Barriers as low as ~0.2 eV can induce significant space-charge region formation across the device, depleting interface carriers and increasing interfacial resistance[43]. High barriers therefore increase R_t and SRH recombination, reducing FF by up to 12%$_{abs}$[43]. While heavily-doping CTLs can mitigate interface carrier depletion, this increases parasitic absorption[174–176]. We therefore recommend designing TCEs with energy barriers to CTLs ~0.1-0.2 eV. Fig. 3b compares the energy levels of typical tandem cell layers with common TCEs. For ETL-TCE contacts, the TCE work function should be ~4-4.5 eV, while at HTL-TCE contacts, it should be ~5-5.4 eV[177,178]. Most TCOs have work function ~4.2-4.6 eV, necessitating modifications to their band structure or to cell design to reduce losses. Additionally, TCO deposition (see Box 2) can degrade cell surfaces and induce Fermi level pinning, further increasing recombination and R_t[46,164]. We next discuss specific perovskite sub-cell interfaces, highlighting strategies to improve energy alignment with TCEs.

Introducing a buffer layer between the TCE and perovskite CTLs can improve band alignment and protect against sputter damage[46–48,179,180]. Buffers must also provide good optical coupling and remain stable to mobile ions[181]. Buffer thickness must balance multiple competing factors: mechanical protection against sputter damage, parasitic optical absorption, and cell series resistance (R_{series})[51,182–186]. In n-i-p perovskites, the most common hole-buffer is ~10 nm thermally-evaporated molybdenum oxide (MoO_x)[51,187–189]. Holes are extracted from HTLs to MoO_x primarily by band transport, but the large MoO_x/TCO interface barrier results in transport into the TCO dominated by lossy trap-assisted-tunnelling. MoO_x absorptance also reduces J_{sc}, and its stoichiometry renders it unstable to moisture/iodide migration[51,183,190–193]. While there has been progress developing more stable, less absorptive hole-buffers such as WO_x, VO_x, MgO_x and CrO_x[34,46,51,183,194], the field is now concentrated on p-i-n architectures, where highly-absorbing HTLs are at the buried rear interface.

At TCO/ETL interfaces in p-i-n perovskite top cells, ALD SnO_x, and to a lesser extent bathocuproine (BCP), are the most common electron-buffers. Ag-NPs in BCP introduce gap

states at 3.74-5.03 eV, enabling efficient direct tunnelling (DT) transport from ETL to TCE[195–199]. However, BCP:Ag suffers from poor damp-heat stability, sputter vulnerability, and delamination at elevated temperature[34,53,200–202]. Compared to BCP, ALD SnO_x offers improved stability to damp-heat, delamination, and ion migration[34,203,204]. ALD SnO_x ~5-10 nm is now near-universal in 2T tandems[181,205–208]. At SnO_x, the energy difference $E_F - E_v$ = 3.6 eV leads to relatively high barriers to most TCEs, meaning transport likely involves lossy thermionic emission and trap-assisted-tunnelling. SnO_x also shows poor stability under strong reverse bias or to solvents, and its ALD precursor (TDMASn) can interact with perovskite at elevated temperatures[49,206,209]. Alternatives require a higher E_c to reduce barriers with TCEs, stability and good optical coupling. Ultimately, achieving stable, high PCE devices may require TCEs capable of direct, lossless CTL contact, potentially eliminating buffer layer requirements. Such TCEs must combine a suitable Φ_{TCE}, interfacial stability, and low-damage deposition.

TCOs can be deposited without damaging underlying layers by tuning sputter power, chamber pressure and temperature[47,164,179,210–214], but such "soft-deposited" TCOs typically have lower conductivity and higher absorptance, leading to a trade-off between TCO quality and damage[164]. Multilayers combining multiple TCEs may facilitate soft deposition, improved band alignment, high conductivity and low absorptance and therefore offer potential to overcome the damage-quality trade-off without using buffer layers[18,81,215]. These multilayers may vary in crystallinity[195], oxygen concentration[216,217], doping[59,218], composition[18], or deposition technique[209,219]. Examples include IZrO on lightly-doped IZO, facilitating a >1.5%$_{abs}$ PCE improvement to 30.74% in a 2T tandem[18], and sputtered ITO on e-beam evaporated In_2O_3, achieving >30% PCE in a 4T tandem[219]. Such improvements can be attributed to improved energy alignment between TCEs and CTLs facilitated by TCE multilayers.

Once inside the TCEs, carriers must be extracted to metal fingers for current collection[9,220,221]. Field-emission transport dominates this interface, and the contact resistance, R_c, is exponentially proportional to the interfacial energy barrier[19,222]. Fig. 3b shows that Ag and Al have a Φ of -4.2-4.5 eV[223–225], and -4.3 eV respectively[225], favourable for most TCOs. Cu, however, has a Φ of ~4.7 eV[226], likely increasing R_c with low-Φ TCEs such as AZO. This mismatch presents a challenge for sustainable Cu-based metallisation[227]. We therefore recommend employing multilayer TCEs or thin metal interlayers to reduce resistance at these interfaces[122,228].

3.2 Recombination Junctions

2T tandem cells require a unique interconnection between sub-cells. For charge neutrality, opposite carriers must recombine at the interconnect. In Fig. 3a this is exemplified where an electron from the silicon recombines with a hole from the perovskite. While TCE-free interconnection is possible via silicon tunnel junctions[38,229] or p^{++} emitter/ETL junctions[230231], their low PCE and manufacturing complexity limit scalability. We therefore focus here on TCE-interconnected tandems.

Most tandems use *n*-type TCOs to form recombination junctions. The energy barrier between TCO and perovskite is often reduced using self-assembled monolayer (SAM) HTLs, including 2PACz, (MeO/Me/Ph/Br)-2PACz, 4-PhCz and (α-Nap/β-Nap/Ph)-PAPT[45,174,178,232–236], reviewed in refs[237–241]. SAM phosphonic acid anchoring groups bind to TCO -OH groups, while SAM terminal groups interact with perovskites[242–244]; the interfacial dipole formed increases the TCO work function[174,242,245]. The work function shift (ΔΦ) depends strongly on TCO microstructure: TCOs with high atomic density, closely-packed planes and many -OH groups such as amorphous IZO induce a higher ΔΦ[242,246–248]. While amorphous interlayers such as NiO_x improve SAM conformity on polycrystalline TCOs, they can reduce V_{oc}[45,177,246,249–251]. Larger shifts can also be achieved by improving SAMs-TCO adhesion using HF, UV-ozone[250], UV plasma[57], oxygen vacancy modulation[252], annealing[253], or SiO_2 nanoparticles (NPs)[254]. However, SAMs tend to suffer from poor damp-heat and adhesion stability, and can

be challenging to deposit on textured surfaces[255], motivating the search for TCOs with intrinsically better HTL band alignment.

In the silicon sub-cell, a low barrier between the TCO and silicon is critical. As in perovskite cells, large barriers can cause space-charge region formation, increasing Schottky barrier height, and SRH recombination[256–258]. Higher silicon doping narrows this region, but increases Auger recombination[257,259]. For *n*-type Si, Φ_{TCE} <4.3 eV is optimal, making ZnO a strong contender with Φ~4.0 eV[256,257]. While increasing TCE doping can reduce Φ_{TCE}, it also increases NIR FCA[258,260,261]. For *p*-type Si, the Φ_{TCE} should be >5.1 eV[257], yet most TCEs have Φ_{TCE}~3.4-4.5 eV[61–63]. Achieving efficient TCE to *p*-Si contacts without excessive FCA remains challenging[258,260,261214]. Crucially, the TCO recombination junction needs to simultaneously contact a perovskite-CTL and silicon-CTL with opposing ideal Φ. An interconnection-TCE with a graded Φ across its thickness may therefore minimise interfacial losses by improving alignment to both sub-cells.

For effective carrier transport, interfacial defect trapping must be minimised. TCO deposition can induce traps[262–264], increasing interface recombination[46,264]. Fortunately, these losses can be partially mitigated through post-deposition annealing. In tunnelling oxide passivated contact (TOPCon) silicon structures, a ~250 °C 10 min forming gas anneal partly re-passivates interface defects after deposition[262,265–269], while in SHJ, annealing at 200 °C for 10 mins can re-passivate and reduce a-Si:H/TCO interface resistance via hydrogen dangling-bond saturation[27,270–274]. But annealing can also filling oxygen vacancies, reducing TCO-doping[263], motivating improved low-damage deposition. Interface losses can also be reduced using TCEs that act as passivating contacts, such as ZnO:H[275–278] or TiO_x[279], which mitigate recombination and enhance carrier selectivity. Such passivating functionalities may also benefit front-TCEs, though this is not yet reported.

While modifying TCE properties can improve band alignment, there is a fundamental dilemma in balancing the need for high lateral resistance to prevent shunting of the top cell, and the need for efficient vertical charge transport for recombination. A relatively low-mobility recombination layer TCE may be beneficial, allowing a wide tuneable range of carrier concentrations to vary its work function without substantially reducing lateral resistance and increasing the risk of shunting. Improved alignment with increased lateral resistance can also be achieved using ultra-thin recombination layers (<5 nm)[45,280]. Lateral conductivity can be tuned in favour of vertical conductivity using TCOs with columnar grains. The relationship between TCO microstructure and optoelectronic properties are discussed in Box 3. But the trade-off goes beyond vertical vs lateral conductivity: target properties must also be balanced in consideration of optical behaviour specific to each interface. The next section addresses strategies to mitigate such optical losses at TCE interfaces across the tandem stack.

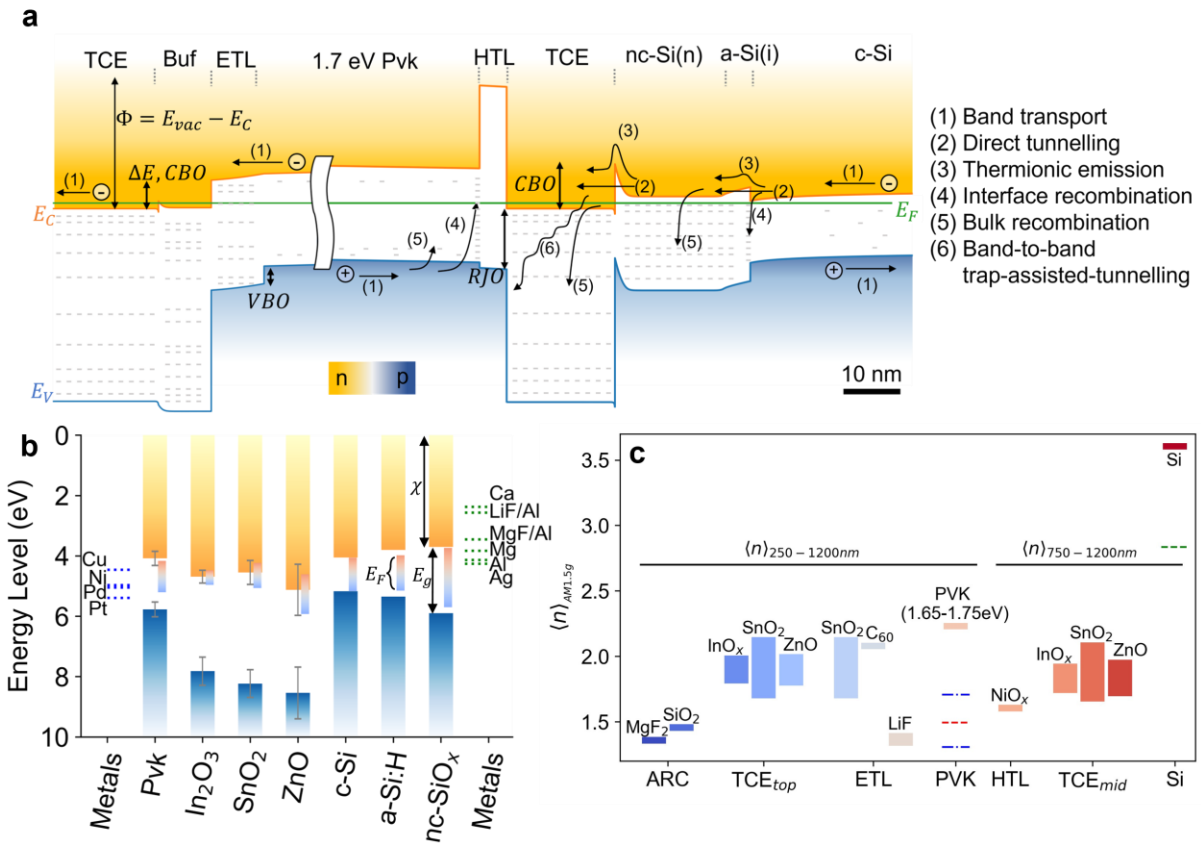

Fig. 3: Energy and optical alignment of TCE interfaces in perovskite-silicon tandem solar cells. **a**. Device band alignment in a two-terminal monolithic perovskite-silicon tandem with n-i-p perovskite and TCE recombination layer. **b**. Energy level diagram of various materials used at each interface in a perovskite-silicon tandem cell. **c**. Refractive indices of various materials used at each interface in a perovskite-silicon tandem cell. The blue and red dotted lines correspond to the ideal refractive indices at air-perovskite interfaces, depending on the anti-reflection coating (ARC) used. The green dotted line corresponds to the ideal refractive index at the perovskite-silicon interface. The data used to plot these figures can be found in the Supplementary Information, Tables S6, S7 and S8.

Box 3: Correlation between microstructure and properties

Microstructure, stoichiometry, and electrical properties are strongly interlinked. TCO films can be amorphous[281], polycrystalline (nano and micro size grains)[242], or less commonly, epitaxial single crystals[282]. Due to substrate constraints, most films used in devices are amorphous or polycrystalline. Both film microstructure and stoichiometry determine the optical and electrical properties, particularly conductivity, which depends on free-carrier concentration and mobility[283].

Larger grains reduce charge-carrier scattering at grain boundaries and lower defect density, enhancing both mobility and transmittance[284,285]. However, achieving large grains typically requires high-temperature processing (> 200 °C). Low temperature processing tends to produce amorphous TCOs dominated by ionised impurity scattering. While defects such as oxygen vacancies can increase carrier density, excessive concentrations can reduce mobility and cause parasitic free-carrier absorption in the near-infrared. Therefore, careful optimisation is needed to balance conductivity, transparency, and thermal compatibility for TCOs in tandem solar cells.

Crystal structure can also influence mobility anisotropy. Heavily-doped TCOs can form a (400) columnar structure that promotes vertical transport, whereas lightly-doped films often form (222) equiaxed grains, favouring lateral transport. Combining these orientations in a multilayer can improve band transport, lateral conductivity and optical coupling, while reducing damage and contact resistance to adjacent layers[18,60,215,286].

Scattering mechanisms in TCO films (AFM images adapted from [242]).

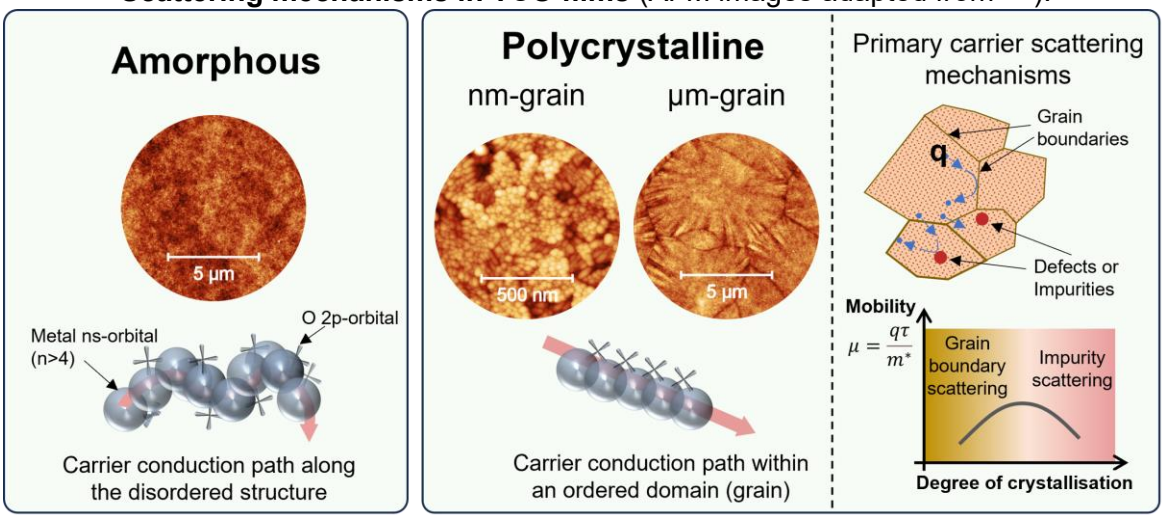

4 Optical Coupling and Absorption Losses

4.1 Optical Matching

When photons are incident on tandem modules, they pass through the glass, encapsulation, antireflection coating (ARC), front-TCE, buffer and CTL, before entering the perovskite absorber. Lower-energy photons continue through the rear CTL and mid-TCE for absorption in the silicon, while some photons are reflected back at the rear-TCE/metal. TCEs must hence be engineered to maximise photon transfer across interfaces, enhancing absorption in both sub-cells to increase short-circuit current densities (J_{sc}). Maximised photogeneration requires consideration of adjacent layers and the distribution of optical fields within them.

In a single solar absorber, photogeneration follows Beer-Lambert's law, with absorption $A_x = I_0(1 - e^{-\alpha x})$, where I_0 is the optical field strength at the sun-facing surface ($x = 0$), α is the wavelength-dependent absorption coefficient, and x is the distance into the absorber. However, in perovskite-silicon tandems, analysis of the optical field distribution (and thus carrier generation profile) must also account for coherent interference of reflected and transmitted waves within each layer and interface[287,288]. Mathematically, the transfer-matrix formalism is used to calculate the electromagnetic field propagation through media, where each matrix describes reflection, transmission, and phase shifts at individual interfaces and layers, incorporating interference effects[289,290]. This approach requires knowledge of the complex refractive index, $\tilde{n} = n + ik$, where the real component, n, governs interference.

Destructive interference at an interface (for a particular wavelength) can be optimised in materials with refractive index n_1 satisfying:

$$n_1 = \sqrt{n_0 n_2}, \quad (4.1)$$

Where n_0 and n_2 are indices of the adjacent media in the device. Fig. 3c depicts the weighted-average refractive indices $\langle n \rangle$ perovskite-silicon tandem layers. As TCE microstructure and doping modify n, a range of values is shown[286]. Particularly apparent is the significant difference between perovskite and silicon $\langle n \rangle$, highlighting that optimal TCE refractive indices strongly depend on position in the device.

The imaginary component k relates to the absorption coefficient, dictating parasitic absorption. As n and k are linked by Kramers-Kronig relations, optimising one affects the other[291–294]. For example, varying doping concentration changes both n and k. TCE design therefore requires balancing refractive-index matching, carrier concentration and absorption losses. Careful measurement of both n and k is essential to identify and mitigate optical coupling losses.

Beyond *ñ* control, absorption decreases with reduced thickness. But to minimise constructive interference and thus reflection, TCE thickness should satisfy the quarter-wavelength condition, $d_{TCE} = \lambda/4n_1$[264]. As each sub-cell absorbs different wavelengths, the optimal TCE thickness varies with interface, and must be carefully balanced with electrical requirements, strongly limiting viable TCEs.

4.2 Photocurrent Loss at the Front-TCE

The front-TCE must maintain high transmittance from 300–1200 nm[295]. While thinner TCEs reduce absorption, this must be considered in conjunction with constructive interference and refractive index matching to adjacent layers and ARCs[86,94,130,194,296]. Following Equation 4.1, the front-TCE n should approximate the geometric mean of the adjacent ARC (n~1.4) and CTL (n~1.6-2)[211,286,297,298]. Several strategies have been employed to reduce front-TCE photocurrent losses. Less absorptive TCOs, such as IZO or IZrO, can replace ITO or FTO, which dominated early 2T and 4T structures[44,299,300]. Mariotti *et al.* showed J_{SC} increases by reducing IZO thickness from 100 nm to 40 nm[86]. Multi-layer TCEs allow independent tuning of optical and electrical properties. For example, Heydarian *et al.* showed that FCA losses can be reduced, without sacrificing carrier transport, using a thin, heavily-doped, low-oxygen TCO, under a thicker, lightly-doped, high-oxygen, TCO[301,302]. Finally, stacking TCOs with differing microstructures can produce a graded refractive index for improved light coupling[286].

4.3 Mid-cell TCEs

Short wavelength photons are absorbed in the perovskite, therefore the mid-TCE transmits primarily ~700-1200 nm light, and its optical performance is dominated by its NIR response. As the refractive index of silicon is >3.5, the ideal mid-TCE n is ~2.8-3, indicated by the green dotted line in Fig. 3c. Recent reports have replaced ITO (n ~1.8) with IZO (n ~2), likely improving optical coupling to silicon. IZrO-based multilayers have been investigated to improve n matching at the front surface of single-junction SHJ cells, offering a promising route to minimise reflection at the perovskite-silicon interface[303]. Alternatively, modifying the underlying micro/nanocrystalline hydrogenated silicon (μ/nc-SiO_x:H) passivation layers can improve n matching[304,177]. Yet, this approach is limited by slow nc-SiO_x:H deposition rates, manufacturing complexity and charge transport limitations[305,306]. Thus, the mid-TCE refractive index remains important for optical coupling at the perovskite-silicon interface. Mid-TCE thickness has steadily reduced to mitigate parasitic absorption, with most reports now using <20 nm TCOs[8,44,130,194,246,269]. Notably, Zheng *et al.* demonstrated that a 1.7 nm ITO layer could serve as an effective mid-TCE on planar surfaces, but precise thickness control <5 nm on textured surfaces remains challenging[45,280].

4.4 Rear-TCEs

At the rear of the device, the TCE must either reflect photons back into silicon, or enable bifacial photoexcitation from rear illumination. Low-E_g TCOs such as AZO or IZO are suitable,

since the rear-side spectrum is primarily >500 nm. IZrO is also frequently used owing to its low IR absorption after ~200 °C annealing[194,307,308]. The rear-TCE is often capped with an aluminium or silver reflector, easing R_{sheet} requirements. However, the metal-TCO contact can introduce parasitic plasmonic absorption[39,309]. This can be alleviated using a low refractive index (n~1.4) dielectric interlayer, preventing the local electromagnetic field from evanescing at the back reflector[69]. Demonstrated approaches include thick MgF_2 or SiO_x layers interspersed with Ag fingers in contact with the TCE[45,306,307,310–312], thin ZnO interlayers[69], silicon nanoparticles[181] and SiO_x-based NPs[254,307]. These approaches require further optimisation for improved silicon IR response, and are difficult to fabricate uniformly on large areas. Developing a rear-TCE with gradient refractive index could further reduce reflection while reducing processing cost and complexity, eliminating the need for additional layers to improve optical coupling.

5 Practical Integration of TCEs in Pvk-Si Tandems

Due to the early stage of perovskite-silicon tandem research, most reported devices are laboratory-scale, with active areas ~1 cm^2. Fig. 4a illustrates the relation between active area, PCE, and indium-based TCE usage in tandems. In research devices, metal contacts lie outside the active area, leaving the front TCO solely responsible for lateral transport[313]. As the active area increases, power losses due to the TCO ($P_{Loss,TCO}$) increase, following:

$$P_{Loss,TCO} = \frac{1}{12} \cdot R_{sheet,TCO} \cdot \frac{J_{MPP}}{V_{MPP}} \cdot W^2$$

where J_{MPP} and V_{MPP} are photocurrent density and voltage at the maximum power point, and W is device width[299,313]. For practical PV modules >200 cm^2, TCE design must incorporate metal fingers that aid lateral conductivity but introduce shading losses. Thus, metal pitch must balance optical/resistance losses[212,264,299,314–316]. Fig. 4b summarises TCE design considerations for upscaling tandems.

For front-TCEs:

1. Addition of metal fingers introduces a trade-off between shading and resistive losses.
2. Low temperature metallisation and TCE deposition are required due to perovskite sensitivity, potentially increasing metal-line resistance, TCE/metal contact resistance or limiting TCE mobility (see Box 2).
3. Low-damage deposition to avoid CTL damage.
4. Low $R_{sheet,TCE}$ to enhance lateral transport and fill factor (*FF*), achieved with thicker TCEs or high mobility to avoid NIR parasitic absorption (see Box 1).

For mid-TCEs:

1. Low damage deposition, avoiding silicon de-passivation. Post-processing annealing may regenerate voltage losses.
2. Reduced thickness, as lateral conductivity is unnecessary[181]. Thin, high R_{sheet} layers suppress shunts, which scale with area due to perovskite inhomogeneity and defects[45].
3. Band alignment to support recombination junction formation, minimising transfer resistance and SRH losses (Fig. 3a).
4. Uniform adhesion to CTLs.

For rear-TCEs:

1. Addition of metal fingers again introduce shading-resistance trade-offs.

2. Integration with intermediate refractive-index layers to minimise plasmonic losses at rear metal reflector.

Across all TCEs:

1. Refractive-index matching with tuned thickness to optimise optical coupling.

2. Reduced indium consumption: 3 TW/yr solar module production requires <0.064 mg/W [7] (Fig. 4a).

In tandems, the current density is lower compared to single-junction cells, reducing resistive losses and relaxing the R_{sheet} requirements for the top and rear-TCEs. However, optically, photocurrent losses have a larger relative impact on power output. To investigate the interplay between electrical and optical losses, we modelled the impact of TCE weighted-average transmittance and R_{sheet} on the ultimate practical perovskite-silicon tandem PCE. The resulting PCE is presented in Fig. 4c. The analysis follows Allen *et al.*, who define a practical PCE target of 37.8%[317]. Chosen parameter details are provided in Supporting Information, Section S.1, following the formalism in ref.[25]. For a typical front-TCE R_{sheet} of 50 Ω/□, a 5% decrease in TCE weighted-average transmittance can cause a > 2%$_{abs}$ PCE loss. This highlights a clear opportunity to increase PCE by developing TCEs with higher weighted-average transmittance.

Another consideration for terawatt-scale tandem production is materials sustainability, particularly indium. Indium is scarce, and is produced almost exclusively as a by-product of other metal ores[9]. Over 70% of global indium is used for ITO production[9], primarily in flat panel displays[9], creating direct competition with the PV industry. Fig. 4d summarises the materials used as the front or interconnection TCEs in perovskite-silicon tandems, showing that indium-based TCEs dominate. Wang *et al.* calculated that a 3 TW/yr tandem manufacturing capacity requires <0.064 mg/W indium consumption[7], as noted in Fig. 4a. Only a handful of reported devices meet this criterion, all at lab-scale dimensions with PCE <18%. Also shown in Fig. 4a is a target of 1.159 mg/W, corresponding to the ITRPV projection for 2030 tandem manufacturing, achieved by limited number of lab-scale tandems. To achieve <0.064 mg/W, the combined indium-containing TCE thickness should be <4 nm. This reliance on indium-based TCEs represents a major bottleneck in scaling high-PCE tandems that must be urgently addressed. In the next section, we explore methods to develop improved low-indium, and indium-free TCEs, providing a roadmap for this bottleneck to be overcome.

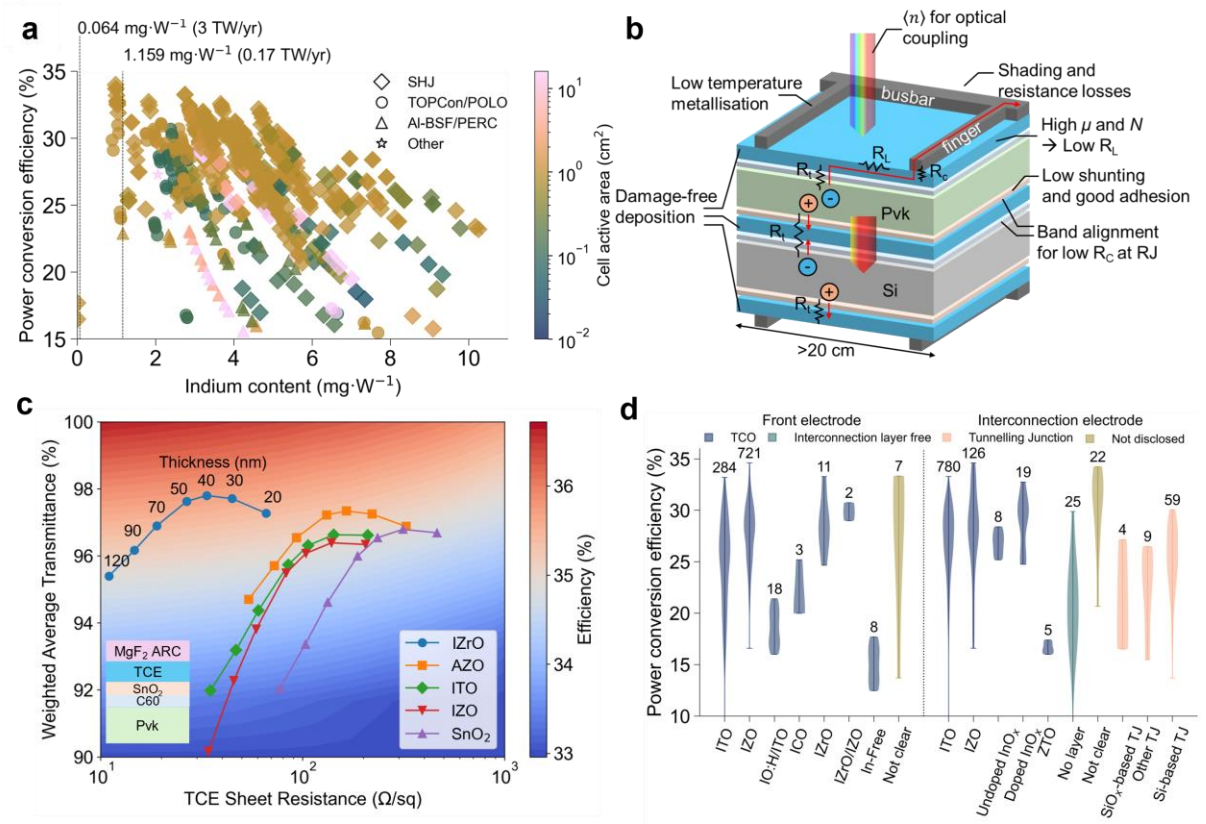

Fig. 4: **TCE sustainability, scalability, integration losses, and material choices in perovskite–silicon tandem solar cells. a**. Indium content per watt of electricity generated in 2T perovskite-silicon tandem cells reported in the literature. Dotted vertical lines at 0.064 mg/W and 1.159 mg/W correspond to the sustainable manufacturing limit for 3 TW/yr and 170 GW/yr respectively. **b**. Losses induced from TCEs in the context of scaling up 2T perovskite-silicon tandems from lab to fab scale. **c**. Predicted PCE based on TCE weighted-average transmittance vs TCE sheet resistance, assuming other losses are eliminated. Each TCE presented here is compared at different thicknesses at intervals from 20 nm on the right, to 120 nm on the left, numerically shown over the IZrO data line in nm. **d**. TCE materials reported at the front and interconnection in 2T monolithic perovskite-silicon tandem cells available online from March 2015 to August 2025. Doped InO_x refers to In_2O_3 doped with W, H, or another undisclosed dopant. Si-based TJs refer to doped nano/micro/poly-crystalline silicon, while SiO_x-based refer to doped nc-SiO_x:H. All other tunnelling junction strategies reported are listed under “Other TJs”. The data used to plot these figures can be found in the Supporting Information, Tables S3, S5, S7 and S8.

6 Outlook

6.1 Strategies for Reducing In Consumption

The reliance of high-PCE tandems on indium has motivated efforts to reduce indium usage in existing TCEs, improve known indium-free TCEs, and develop entirely new indium-free TCEs. Perovskite-on-TOPCon is an immediate route to reduce indium consumption, eliminating the rear-TCE, and already achieving >30% PCE. Typical ITO and IZO sputter targets contain 90% In_2O_3. A 35% PCE perovskite-on-TOPCon tandem requiring 35-60 nm indium-based TCEs, therefore corresponds to ~0.7-1.1 mg/W In, enabling ~180-280 GW/yr sustainable manufacturing. Recently it was shown that $Zn_3In_2O_6$ targets can reduce indium usage in IZO by 50% without compromising optoelectronic properties[58], potentially increasing capacity to a maximum of ~560 GW/yr. Achieving high PCE at TW-scale will therefore likely require tandems using indium-free TCEs only.

Existing indium-free TCEs, including AZO, GZO, and FTO have not been reported in high-PCE tandems due to high FCA, low mobility, poor stability, poor band alignment or deposition constraints. In the short term, multilayers combining indium-based with indium-free TCEs could reduce In-consumption. AZO with high R_{sheet} could serve as an interconnect TCE, with a thin indium-based interlayer to improve band alignment to the perovskite-HTL, inhibit ion migration, and limit deleterious ZnO-perovskite reactions. At the front-TCE, achieving low R_{sheet} indium-free TCOs with low absorptance remains challenging due to their low mobility. While hybrid nanocomposites, 2D materials, and MXenes[75,76] may offer scope to reduce indium-consumption and provide passivation, they cannot yet be deposited conformally on textured surfaces with sufficient optoelectronic quality, stability and processing compatibility for high-PCE 2T tandems[76–78,161]. There is therefore strong motivation to develop novel indium-free TCOs, compatible with tandem-cell processing, stability and optoelectronic property requirements.

6.2 Atomistic Modelling for Indium-Free TCO Development

Density functional theory (DFT) is central to indium-free TCO development, particularly with recent improvements in high-throughput screening via deep learning, and treatments of forbidden transitions and polaronic conduction[67,88,318]. However, predictions assume ideal bulk crystals, while practical TCEs are thin films fabricated under non-equilibrium conditions with often high defect densities. This can lead to properties deviating significantly from predictions due to surface energies, strain, and microstructure. For example, bulk single-crystal La:$BaSnO_3$ exhibits >300 cm^2/Vs mobility, yet thin films, requiring >700 °C deposition, achieve only ~80 cm^2/Vs[319–321]. Researchers often abandon materials after one unsuccessful synthesis approach, highlighting the need to consider synthesisability when screening[84]. Machine learning and artificial intelligence can guide materials design, but models remain limited by the quality and completeness of training data. Progress requires more rigorous reporting of experimentally-measured TCO properties, which is often lacking for less-studied materials.

DFT recently predicted several high-mobility indium-free TCEs exploiting resonant doping[65,66,322]. In Ta:SnO_2, the resonance of the Ta 5*d* states in the SnO_2 CB yields a low m^* of 0.23 m_0. Ta:SnO_2 thin films exhibit μ~20 cm^2/Vs, Φ~4.66 eV, and R_{sheet} ~190 Ω/□, enabling SHJ integration with >25% PCE[322–324]. Ta:SnO_2 could function as a perovskite-silicon interconnect due to its high Φ and moderate R_{sheet}, but requires controlled low thicknesses deposition. Several promising predicted TCEs remain unfabricated as thin films: Ga:$ZnSb_2O_6$[100], F:Sb_2O_5[325] and $KSbO_3$. Ga:$ZnSb_2O_6$ shows promise as an interconnection layer, where its high Φ~6 eV could improve band alignment to the perovskite E_V without SAMs[100]. F:Sb_2O_5 offers low absorptance and high mobility, potentially suited as a front-TCE[325]. Even if non-toxic themselves, the toxicity of intermediate antimony-based compounds such as Sb_2O_3 should be considered during fabrication and lifetime degradation[326]. Additional low m^* materials unfabricated as thin films include $BeSiP_2$, and GeO_2[318], but sustainability considerations for Be and Ge may limit large-scale applicability[327,328].

For perovskite-silicon tandems, modelling should prioritise band alignment and passivation, reducing dependence on buffer layers and SAMs, while improving PCE and stability. Optically, front-TCEs should have low n~1.5-1.75, but mid and rear-TCEs should have high n~2-3. Low broadband absorptance should be prioritised over low R_{sheet} as R_{sheet} constraints are relaxed in tandems relative to single-junction cells. Crystallisation kinetics are a key bottleneck in fabricating DFT-predicted TCEs as thin films. To support experimentalists, atomistic simulations could be used to predict upper mobility limits and crystallisation mechanisms for candidate materials. Improved structural understanding of TCEs deposited under different conditions, via high-energy techniques such as x-ray absorption spectroscopy could provide the needed data for improved predictions. As these mechanisms involve complex interatomic

and microstructural interactions, AI-assisted modelling can provide valuable insights by iteratively screening potential growth pathways across large datasets.

6.3 Exploiting Nanophotonics to Improve TCE Performance

Beyond developing new TCEs, nanophotonic structures can complement TCEs, providing light-trapping beyond the Lambertian limit[329]. At the front-TCE, reflection can be reduced by embedding in it SiO_2-NPs, lowering n[330], or incorporating Al-nanospheres, which enhance local surface plasmon resonance[70]. Although demonstrated for mid and rear-TCEs, the stringent requirements of the front-TCE make integration challenging[254,307,71]. At the mid-TCE, embedded plasmonic metamaterial Ag-NPs or nanocones can be tuned to increase reflection <500 nm back to the perovskite, while transmitting near-IR to the silicon[72,73]. Such enhancements may enable indium-free TCOs whose poor electrical and optical properties are compensated by nanophotonics.

6.4 *p*-type TCEs

All TCEs used in tandems are currently *n*-type. *p*-type TCOs could simplify device design, replacing the HTL/*n*-TCO/buffer with a single *p*-TCO aligned to the perovskite E_v[84], as well as reducing dependence on indium-based *n*-TCEs. However, *p*-type TCO design faces a contradiction in requirements: achieving high *p*-type conductivity via hole mobility and low ionisation potential, while maintaining transparency via a wide bandgap. In most metal oxides, the VB consists of localised oxygen 2*p* orbitals. This VB character, along with oxygen's electronegativity, leads to a flat dispersion and large hole effective mass, limiting hole mobility[88,103,331,332]. We refer readers to comprehensive reviews on *p*-type TCEs[84,331,333], but briefly highlight the most promising materials. DFT predicts promising *p*-type oxides (Ta_2SnO_6, Ba_2BiTaO_6 and $K_2Sn_2O_3$) but they remain difficult to fabricate with good microstructure and low defect density at low-temperatures[84]. Several *p*-type oxides have been used as HTLs (NiO_x or SnO_2:Sb[334]) thanks to their high work function, but their R_{sheet} is insufficient for TCE application. Conversely, Cu_2O films offer moderate conductivity, but insufficient transmittance, reducing J_{sc} in PV devices[335–337].

Chemical modulation of the VB has been explored to increase hole mobility and facilitate *p*-type doping, as demonstrated in low-temperature fabricated CuI and S-doped or alloyed CuI[338–340]. BP and CaCuP are also proposed dispersed-VB *p*-TCEs, but require deposition temperature >400 °C[341,342]. While the performance of *p*-TCEs still lags that of *n*-TCEs, these dispersed-VB halide, sulphide and phosphide materials show promise. Bridging the gap between prediction and fabrication through more robust structural analysis may be the key to achieve practical integration of *p*-TCEs in high-PCE tandems[82,325,327]

6.5 Research Roadmap for Next Generation TCEs for Tandems

Table 1 summarise the target TCE properties for tandem cells, highlighting opportunities across optics, electronics, processing and sustainability. We focus on p-i-n lead-halide perovskite on silicon structures, the dominant and most commercially relevant architecture, though the underlying analysis extends to future multi-junction tandems with many, differing absorbers. This provides a roadmap for next-generation TCE development for rapid translation and application to optoelectronic devices. We emphasise the importance of examining the physics of each interface in developing TCEs, where the ideal properties and trade-offs may diverge substantially. Careful consideration of these requirements will be key to achieve multi-junction tandem cells with efficiency approaching their theoretical limits >40%.

644 **Table 1:** Strategies for TCE development for high efficiency sustainable p-i-n lead-halide perovskite on silicon tandem cells.

		TCE Location		
		Front	**Middle**	**Rear (SHJ only)**
	Current materials	*IZO, ITO, IZrO*	*ITO, IZO*	*ITO, IZO*
	Thickness (nm)	*20-50*	*5-15*	*50-150*

Optics	**Role**	*Optical coupling from air-Pvk.*	*Optical coupling from Pvk-Si.*	*Bifacial: Si-air coupling. Monofacial: Si back-reflector, minimise plasmonic losses.*
	Weighted absorptance (%)	Ideal: <0.01%, 300-1200 nm. Actual: ~0.5-3%.	Ideal: <0.01%, 750-1200 nm. Actual: ~0.01-0.05%.	Ideal: <0.01%, 750-1200 nm. Actual: ~0.1%.
	Weighted real refractive index (n)	Ideal: 1.5-1.75 (depending on ARC used), 300-1200 nm. Actual: ~1.8-2.2.	Ideal: 2.8-3, 750-1200 nm. Actual: ~1.8-2.2.	Bifacial: 1.9-2.3, 750-1200 nm. Monofacial: 2.8-3.0, 600-1200 nm. Actual: ~1.8-2.2.
	Challenges	Near-UV, IR absorption, reflection.	IR absorption, reflection.	IR absorption, albedo reflection.
	Development opportunities	Graded refractive index. Nanophotonic structures. High mobility TCOs.	Graded refractive index. Plasmonic materials. Metamaterials.	Variable refractive index interlayers.

Electrical	**Role**	*Low vertical and lateral R_{series}*	*Recombine carriers from both sub-cells, and high R_{shunt}*	*Low vertical and lateral R_{series}*
	R_{sheet} (Ω/□)	Ideal: <20. Actual: ~50-100.	Ideal: ~200-1000. Actual: ~1000.	Ideal: <50. Actual: <50.
	Φ (eV)	Ideal: 4.0-4.7. Actual: 4.2-4.6.	Ideal: >5.0 (Pvk-HTL), <4.3 (n-Si). Actual: 4.2-4.6.	Ideal: >5.1. Actual: 4.2-4.6.
	Challenges	Lateral resistance. ETL band alignment. Cu band alignment (ideal 4.7 eV).	Perovskite HTL band alignment. Conformality, uniformity and shunting resistance. Si interface de-passivation.	Silicon p-type band alignment and lateral conductivity.
	Development opportunities	High mobility TCOs. TCEs with graded work function to align with both ETL and metal fingers.	p-type TCEs. Buffer layers. Multilayer with graded work function for electrical coupling.	p-type TCEs.

Processing	Deposition conditions	Low deposition energy, <150 ℃.	<250 ℃, SHJ. <500 ℃, TOPCon. Conformality on textured substrates.	<250 ℃
	Chemical barrier	Prevent metal ingress (Ag, Cu), halide ion egress.	Prevent halide ion egress.	Prevent metal ingress (Al, Ag, Cu).
	Interface stability challenges	Stable to perovskite degradation, metal contacts.	Stable to perovskite degradation.	Stable to metal contacts.
	Challenges	Perovskite instability to Zn. Low temperature, low-damage deposition of high-mobility TCOs. Compatibility with metallisation techniques.	Perovskite instability to Zn. Low temperature, low-damage deposition of high-mobility TCOs. Si interface passivation.	Temperature limitations. Contact stability.
	Development opportunities	Soft deposition by RPD, ALD, etc. 2D material ion barriers	2D materials ion barriers. Buffer layers.	Buffer layers.

Strategies for improved TCEs	Sustainable alternatives	AZO, GZO, Ga:$ZnSb_2O_6$, F:Sb_2O_5 perhaps in multilayer with thin (<4nm) In_2O_3 layer. Metal NWs with ALD TCO coatings. Nanophotonic structuring	Low-temperature SnO_2-based TCO, or doped ZnO such as Ga:$ZnSb_2O_6$ with suitable buffer layer.	AZO, GZO with variable refractive index interlayers.

	Short term ↓ ↓ ↓ Long term application	Improved deposition for multilayer TCEs with gradient properties at the nanoscale (doping, crystallinity) and hydrogen doping control. Novel ALD precursor and sputter target development for reduced In use. AI-assisted prediction and deposition of novel TCE materials. Modelling crystallisation dynamics to improve fabrication of predicted TCE materials.

6.6 Conclusions

Currently available TCEs remain a significant source of energy loss in perovskite-silicon tandems, while also increasing cost and limiting sustainability. High-efficiency tandems remain dependent on ITO and IZO, restricting deployment to <0.2 TW/yr due indium reliance, and introduce losses including parasitic UV/IR absorption, reflection, and interfacial band misalignment. Existing indium-free alternatives such as AZO and FTO face challenges in band alignment, stability, and optical losses. Addressing these issues will likely require moving beyond single-material TCEs towards multi-pronged strategies to better balance the trade-off between TCE requirements at different interfaces. We highlight opportunities to engineer graded-property multi-layers that minimise reflection while improving energy level alignment. Developments in low-damage, conformal deposition, such as spatial ALD, pulsed laser and reactive plasma deposition may improve dopant control, hydrogen concentration and crystallisation at the nanoscale, and could enable stable metal NW integration with appropriate band alignment.

In the longer term, integrating TCOs with 2D materials that provide ion barrier and passivation properties such as graphene and MXenes may prove beneficial, if they can be deployed economically across large areas. Looking forward, we expect optoelectronic simulation and machine learning to accelerate discovery of suitable materials and precursors. Improved, high-throughput DFT screening, spectroscopic analysis and soft-deposition methods may expand the accessible material set for deposition on delicate perovskite and a-Si layers. Overall, we recommend closer examination of interface physics within the tandem stack when designing new TCE materials, to accelerate translation of theoretically predicted indium-free TCEs to practical devices. This improved understanding can be directly applied to multi-junction all-perovskite, perovskite/CIGS and organic PV tandems, as well as other optoelectronic devices such as LEDs and photodetectors.

7 Acknowledgements

R.S.B was supported by the Leverhulme Prize for Engineering (PLP-2022-154). This work was supported by the UK Engineering and Physical Sciences Research Council grant number EP/X037169/1 and by the Oxford University John Fell Fund. This work was funded by UK Research and Innovation (UKRI) under the UK government's Horizon Europe funding guarantee grant number EP/Y027884/1.. J.O. acknowledges support through the UK Engineering and Physical Sciences Research Council Doctoral Prize Fund, and Impact Acceleration Account Award (Grant No. EP/X525777/1). A. S. and R. L. Z. H. thank support from St. John's College Oxford for support through the visiting researcher scheme. A.S. acknowledges the Agence Nationale de la Recherche (ANR, France) for support via the project ANR-23-CE51-0029-01 "INNOVATION". A.S. would like to thank Toulouse INP for the ETI POLYTANCE project and the CNRS for the PROCEDO project. This work was partially supported by the "PHC PESSOA" programme (project number: 52869ZM). R.L.Z.H. thanks UK Research and Innovation for support through a Frontier Grant (Grant No. EP/X029900/1), awarded through the 2021 European Research Council (ERC) Starting Grant scheme, as well as the Engineering and Physical Sciences Research Council for financial support (Grant No. EP/V014498/2). R.L.Z.H. also thanks the Royal Academy of Engineering and the Science and Technology Facilities Council for support through a Senior Research Fellowship (Grant No. RCSRF/2324-18-68). M.M.M. and P.L. acknowledge the support from the CETPartnership

EPoBoC project (cetp-2022-00297). All authors are grateful to Bart Macco at TU Eindhoven for providing the base resistivity data set from his ALD-TCE review paper.

8 Data Availability

All data created during this research and published in this article is openly available as tabulated datasets and can be downloaded from the Oxford University Research Archive free of charge from http://ora.ox.ac.uk. For the purpose of Open Access, the author has applied a CC BY public copyright licence to any Author Accepted Manuscript (AAM) version arising from this submission

9 References

1. Richter, A., Hermle, M. & Glunz, S. W. Reassessment of the limiting efficiency for crystalline silicon solar cells. *IEEE J Photovolt* **3**, 1184–1191 (2013).

2. Niewelt, T. *et al.* Reassessment of the intrinsic bulk recombination in crystalline silicon. *Solar Energy Materials and Solar Cells* **235**, 111476 (2022).

3. Green, M. A. & Zhou, Z. Improved silicon solar cells by tuning angular response to solar trajectory. *Nature Communications* **16**, 1–8 (2025).

4. 27.81%! LONGi Refreshes the World Record for the Efficiency of Monocrystalline Silicon Cells Again. https://www.longi.com/us/news/longi-world-record-efficiency-of-monocrystalline-silicon-cells/.

5. Wang, G. *et al.* Silicon solar cells with hybrid back contacts. *Nature* **647**, 369–374 (2025).

6. Schygulla, P. *et al.* Quadruple Junction Solar Cell with 47.6 % Conversion Efficiency under Concentration. Preprint at https://publica.fraunhofer.de/handle/publica/436210 (2022).

7. Wang, L. *et al.* Sustainability evaluations on material consumption for terawatt-scale manufacturing of silicon-based tandem solar cells. *Progress in Photovoltaics: Research and Applications* **31**, 1442–1454 (2023).

8. Aydin, E. *et al.* Pathways toward commercial perovskite/silicon tandem photovoltaics. *Science* **383**, eadh3849 (2024).

9. Zhang, Y., Kim, M., Wang, L., Verlinden, P. & Hallam, B. Design considerations for multi-terawatt scale manufacturing of existing and future photovoltaic technologies: challenges and opportunities related to silver, indium and bismuth consumption. *Energy Environ Sci* **14**, 5587–5610 (2021).

10. Wilson, G. M. *et al.* The 2020 photovoltaic technologies roadmap. *J Phys D Appl Phys* **53**, 493001 (2020).

11. Haegel, N. M. *et al.* Terawatt-scale photovoltaics: Transform global energy Improving costs and scale reflect looming opportunities. *Science* **364**, 836–838 (2019).

12. Best Research-Cell Efficiency Chart | Photovoltaic Research | NREL. https://www.nrel.gov/pv/cell-efficiency.html.

13. 34.85%! LONGi Breaks World Record for Crystalline Silicon-Perovskite Tandem Solar Cell Efficiency Again - LONGi. https://www.longi.com/en/news/silicon-perovskite-tandem-solar-cells-new-world-efficiency/.

14. Filipič, M. *et al.* CH3NH3PbI3 perovskite / silicon tandem solar cells: characterization based optical simulations. *Opt Express* **23**, A263 (2015).

15. Mailoa, J. P. *et al.* A 2-terminal perovskite/silicon multijunction solar cell enabled by a silicon tunnel junction. *Appl Phys Lett* **106**, 121105 (2015).

16. LONGi sets a new world record of 33.9% for the efficiency of crystalline silicon-perovskite tandem solar cells -LONGi. https://www.longi.com/en/news/new-world-record-for-the-efficiency-of-crystalline-silicon-perovskite-tandem-solar-cells/.

17. 34.6%! Record-breaker LONGi Once Again Sets a New World Efficiency for Silicon-perovskite Tandem Solar Cells. https://www.longi.com/en/news/2024-snec-silicon-perovskite-tandem-solar-cells-new-world-efficiency/.

18. Han, W. *et al.* IZrO/IZO multilayer thin film as transparent electrode in perovskite/silicon tandem solar cell. *J Power Sources* **644**, 237048 (2025).

19. Morales-Masis, M., De Wolf, S., Woods-Robinson, R., Ager, J. W. & Ballif, C. Transparent Electrodes for Efficient Optoelectronics. *Adv Electron Mater* **3**, 1600529 (2017).

20. Verlinden, P. J. Future challenges for photovoltaic manufacturing at the terawatt level. *Journal of Renewable and Sustainable Energy* **12**, 053505 (2020).

21. Sofia, S. E. *et al.* Roadmap for cost-effective, commercially-viable perovskite silicon tandems for the current and future PV market. *Sustain Energy Fuels* **4**, 852–862 (2020).

22. Wang, Q., Lyu, M., Zhang, M., Yun, J. H. & Wang, L. Configuration-centered photovoltaic applications of metal halide perovskites. *J Mater Chem A Mater* **5**, 902–909 (2017).

23. Moeini, S., Noori, M. & Abbasiyan, A. Efficiency enhancement in 4T perovskite/Si tandem solar cell by charge extraction management. *Solar Energy Materials and Solar Cells* **285**, 113510 (2025).

24. O'Sullivan, J. *et al.* Towards a graphene transparent conducting electrode for perovskite/silicon tandem solar cells. *Progress in Photovoltaics: Research and Applications* **31**, 1478–1492 (2023).

25. Sebastian Bonilla, R. The Impact of Transparent Conducting Electrodes on Tandem Solar Cell Efficiency. *Joule* 102211 (2025) doi:doi.org/10.1016/j.joule.2025.102211.

26. Islam, M. A. U., Kato, T., Kato, S. & Soga, T. Effectiveness of 2-Terminal Perovskite/Perovskite/c-Si Triple-Junction Solar Cells: An Integrated Study with an Emphasis on Methylammonium Bismuth Iodide. *ACS Appl Mater Interfaces* **16**, 53904–53917 (2024).

27. Li, F. *et al.* Highly Efficient Monolithic Perovskite/Perovskite/Silicon Triple-Junction Solar Cells. *Advanced Materials* **36**, 2311595 (2024).

28. Haacke, G. New figure of merit for transparent conductors. *J Appl Phys* **47**, 4086 (2008).

29. Jain, V. K. & Kulshreshtha, A. P. Indium-Tin-Oxide transparent conducting coatings on silicon solar cells and their "figure of merit". *Solar Energy Materials* **4**, 151–158 (1981).

30. Cisneros-Contreras, I. R., Muñoz-Rosas, A. L. & Rodríguez-Gómez, A. Resolution improvement in Haacke's figure of merit for transparent conductive films. *Results Phys* **15**, 102695 (2019).

31. Mendez-Gamboa, J. A., Castro-Rodriguez, R., Perez-Quintana, I. V., Medina-Esquivel, R. A. & Martel-Arbelo, A. A figure of merit to evaluate transparent conductor oxides for solar cells using photonic flux density. *Thin Solid Films* **599**, 14–18 (2016).

32. Anand, A., Islam, M. M., Meitzner, R., Schubert, U. S. & Hoppe, H. Introduction of a Novel Figure of Merit for the Assessment of Transparent Conductive Electrodes in Photovoltaics: Exact and Approximate Form. *Adv Energy Mater* **11**, 2100875 (2021).

33. Lamanna, E. *et al.* Mechanically Stacked, Two-Terminal Graphene-Based Perovskite/Silicon Tandem Solar Cell with Efficiency over 26%. *Joule* **4**, 865–881 (2020).

34. Hou, F. *et al.* Monolithic perovskite/silicon tandem solar cells: A review of the present status and solutions toward commercial application. *Nano Energy* **124**, 109476 (2024).

35. Jacobs, D. A. *et al.* Light Management: A Key Concept in High-Efficiency Perovskite/Silicon Tandem Photovoltaics. *Journal of Physical Chemistry Letters* **10**, 3159–3170 (2019).

36. Jiang, Y. *et al.* Optical analysis of perovskite/silicon tandem solar cells. *J Mater Chem C Mater* **4**, 5679–5689 (2016).

37. Er-Raji, O. *et al.* Loss Analysis of Fully-Textured Perovskite Silicon Tandem Solar Cells: Characterization Methods and Simulation toward the Practical Efficiency Potential. *Solar RRL* **7**, 2300659 (2023).

38. Ying, Z., Yang, X., Wang, X. & Ye, J. Towards the 10-Year Milestone of Monolithic Perovskite/Silicon Tandem Solar Cells. *Advanced Materials* **36**, 2311501 (2024).

39. Turkay, D. *et al.* Self-Aligned Silica Nanoparticle Rear Reflectors for Single-Junction Si and Perovskite-Si Tandem Solar Cells. *Solar RRL* **9**, 2400704 (2025).

40. Wright, M. *et al.* Design considerations for the bottom cell in perovskite/silicon tandems: a terawatt scalability perspective. *Energy Environ Sci* **16**, 4164–4190 (2023).

41. Klein, A. *et al.* Transparent Conducting Oxides for Photovoltaics: Manipulation of Fermi Level, Work Function and Energy Band Alignment. *Materials* **3**, 4892–4914 (2010).

42. Luderer, C., Messmer, C., Hermle, M. & Bivour, M. Transport Losses at the TCO/a-Si:H/c-Si Heterojunction: Influence of Different Layers and Annealing. *IEEE J Photovolt* **10**, 952–958 (2020).

43. Walter, D., Peng, J., Weber, K., Catchpole, K. R. & White, T. P. Performance limitations imposed by the TCO heterojunction in high efficiency perovskite solar cells. *Energy Environ Sci* **15**, 5202–5216 (2022).

44. Aydin, E. *et al.* Zr-Doped Indium Oxide (IZRO) Transparent Electrodes for Perovskite-Based Tandem Solar Cells. *Adv Funct Mater* **29**, 1901741 (2019).

45. Aydin, E. *et al.* Enhanced optoelectronic coupling for perovskite/silicon tandem solar cells. *Nature* **623**, 732–738 (2023).

46. Aydin, E. *et al.* Sputtered transparent electrodes for optoelectronic devices: Induced damage and mitigation strategies. *Matter* **4**, 3549–3584 (2021).

47. Härtel, M. *et al.* Reducing sputter damage-induced recombination losses during deposition of the transparent front-electrode for monolithic perovskite/silicon tandem solar cells. *Solar Energy Materials and Solar Cells* **252**, 112180 (2023).

48. Demaurex, B., De Wolf, S., Descoeudres, A., Charles Holman, Z. & Ballif, C. Damage at hydrogenated amorphous/crystalline silicon interfaces by indium tin oxide overlayer sputtering. *Appl Phys Lett* **101**, 171604 (2012).

49. Xu, Z. *et al.* Reverse-bias resilience of monolithic perovskite/silicon tandem solar cells. *Joule* **7**, 1992–2002 (2023).

50. Bogachuk, D. & Feldmann, F. Do perovskites need silicon to be stable under reverse bias? *Joule* **7**, 2423–2426 (2023).

51. Bush, K. A. *et al.* Thermal and Environmental Stability of Semi-Transparent Perovskite Solar Cells for Tandems Enabled by a Solution-Processed Nanoparticle Buffer Layer and Sputtered ITO Electrode. *Advanced Materials* **28**, 3937–3943 (2016).

52. Boyd, C. C. *et al.* Barrier Design to Prevent Metal-Induced Degradation and Improve Thermal Stability in Perovskite Solar Cells. *ACS Energy Lett* **3**, 1772–1778 (2018).

53. Chen, P. *et al.* The Promise and Challenges of Inverted Perovskite Solar Cells. *Chem Rev* **124**, 10623–10700 (2024).

54. Liu, H. *et al.* Transparent Conductive Oxide Films and Their Applications in Silicon Heterojunction and Perovskite/Silicon Tandem Photovoltaics. *ACS Appl Energy Mater* **8**, 4032–4047 (2025).

55. Haegel, N. M. *et al.* Photovoltaics at multi-terawatt scale: Waiting is not an option. *Science* **380**, 39–42 (2023).

56. Wagner, L. *et al.* The resource demands of multi-terawatt-scale perovskite tandem photovoltaics. *Joule* **8**, 1142–1160 (2024).

57. Guo, R. *et al.* Degradation mechanisms of perovskite solar cells under vacuum and one atmosphere of nitrogen. *Nat Energy* **6**, 977–986 (2021).

58. Gao, Z. *et al.* Source Material Design for Realizing >50% Indium-Saving Transparent Electrode toward Sustainable Development of Silicon Heterojunction Solar Cells. *ACS Appl Mater Interfaces* **17**, 3265–3277 (2025).

59. Voisin, L., Ohtsuka, M., Petrovska, S., Sergiienko, R. & Nakamura, T. Multilayer indium saving ITO thin films produced by sputtering method. *J Alloys Compd* **827**, 154378 (2020).

60. Yan, Z. *et al.* Gallium-Doped Zinc Oxide/Tungsten-Doped Indium Oxide Stacks with Enhanced Lateral Transport Capability for Efficient and Low-Cost Silicon Heterojunction Solar Cells. *Solar RRL* **8**, 2301029 (2024).

61. Wang, J. *et al.* Application of Indium Tin Oxide/Aluminum-Doped Zinc Oxide Transparent Conductive Oxide Stack Films in Silicon Heterojunction Solar Cells. *ACS Appl Energy Mater* **4**, 13586–13592 (2021).

62. Dong, G. *et al.* Highly efficient silicon heterojunction solar cells with ZnO:Al transparent electrode and transition metal doped indium oxide interfacial layer. *Progress in Photovoltaics: Research and Applications* **31**, 931–938 (2023).

63. Tang, Q. *et al.* > 85% indium reduction for high-efficiency silicon heterojunction solar cells with aluminum-doped zinc oxide contacts. *Solar Energy Materials and Solar Cells* **251**, 112120 (2023).

64. Mercaldo, L. V. *et al.* Monolithic perovskite/silicon-heterojunction tandem solar cells with nanocrystalline Si/SiOx tunnel junction. *Energies (Basel)* **14**, 7684 (2021).

65. Liu, C. P. *et al.* Resonant transition metal Ti or Ta doping in high mobility transparent conducting CdO: The effects of doping concentration. *Phys Rev Mater* **8**, 044603 (2024).

66. Swallow, J. E. N. *et al.* Resonant doping for high mobility transparent conductors: the case of Mo-doped In2O3. *Mater Horiz* **7**, 236–243 (2020).

67. Brunin, G., Rignanese, G. M. & Hautier, G. High-performance transparent conducting oxides through small-polaron transport. *Phys Rev Mater* **3**, 064602 (2019).

68. Exarhos, G. J. & Zhou, X.-D. Discovery-based design of transparent conducting oxide films. *Thin Solid Films* **515**, 7025–7052 (2007).

69. Huang, Q. *et al.* Plasmonic modulated back reflector for thin film photovoltaics. *Solar Energy Materials and Solar Cells* **225**, 110997 (2021).

70. Song, Z. *et al.* Design of high efficiency perovskite/silicon tandem solar cells based on plasmonic enhancement of metal nanosphere. *Acta Physica Sinica* **71**, 038801–1 (2022).

71. Abbasiyan, A. & Golmohammadi, S. Bifacial perovskite/silicon tandem solar cell with Ag nanoparticles as an intermediate layer. *Phys Scr* **100**, 035507 (2025).

72. Kim, K. *et al.* Are nanophotonic intermediate mirrors really effective in enhancing the efficiency of perovskite tandem solar cells? *Nanophotonics* **14**, 1239-1248. (2025).

73. Hu, C. *et al.* Theoretical Analysis of Perovskite/Ultrathin Silicon Tandem Solar Cells with Ag Nanocone Plasmonics. *Plasmonics* https://doi.org/doi.org/10.1007/s11468-025-02975-9 (2025) doi:doi.org/10.1007/s11468-025-02975-9.

74. Mendes, M. J. *et al.* Optimal-Enhanced Solar Cell Ultra-thinning with Broadband Nanophotonic Light Capture. *iScience* **3**, 238–254 (2018).

75. Ferrera, M., Saha, S., Boltasseva, A., Shalaev, V. M. & Jaffray, W. Transparent conducting oxides: from all-dielectric plasmonics to a new paradigm in integrated photonics. *Adv Opt Photonics* **14**, 148–208 (2022).

76. Han, T. *et al.* MXene-Interconnected Two-Terminal, Mechanically-Stacked Perovskite/Silicon Tandem Solar Cell with High Efficiency. *Adv Funct Mater* **34**, 2311679 (2024).

77. Kanti, P. K., K., D. J., Swapnalin, J. & Vicki Wanatasanappan, V. Advancements and prospects of MXenes in emerging solar cell technologies. *Solar Energy Materials and Solar Cells* **285**, 113540 (2025).

78. Raoui, Y. *et al.* Synergic MXene and S-benzyl-L-cysteine Passivation Strategies for Wide Bandgap Perovskite Solar Cells for 4T Tandem Applications. *Small* **21**, 2411310 (2025).

79. Zhang, Q., Chen, X., Lim, E. L., Shi, L. & Wei, Z. Advancing all-perovskite two-terminal tandem solar cells: optimization of wide- and narrow-bandgap perovskites and interconnecting layers. *Energy Environ Sci* **18**, 3060–3084 (2025).

80. Liu, L. *et al.* Advancements and Challenges in Wide-Bandgap Perovskite Solar Cells: From Single Junction to Tandem Solar Cells. *Solar RRL* **8**, 2400359 (2024).

81. Shao, Y. *et al.* Innovations in Interconnecting Layers for Perovskite-Based Tandem Solar Cells. *ACS Energy Lett* **9**, 4892–4921 (2024).

82. Edwards, P. P., Porch, A., Jones, M. O., Morgan, D. V. & Perks, R. M. Basic materials physics of transparent conducting oxides. *Dalton Transactions* 2995–3002 (2004) doi:10.1039/B408864F.

83. Chopra, K. L., Major, S. & Pandya, D. K. Transparent conductors-A status review. *Thin Solid Films* **102**, 1–46 (1983).

84. Woods-Robinson, R., Morales-Masis, M., Hautier, G. & Crovetto, A. From Design to Device: Challenges and Opportunities in Computational Discovery of p -Type Transparent Conductors . *PRX Energy* **3**, 031001 (2024).

85. Dixon, S. C., Scanlon, D. O., Carmalt, C. J. & Parkin, I. P. n-Type doped transparent conducting binary oxides: an overview. *J Mater Chem C Mater* **4**, 6946–6961 (2016).

86. Mariotti, S. *et al.* Interface engineering for high-performance, triple-halide perovskite–silicon tandem solar cells. *Science* **381**, 63–69 (2023).

87. Sze, S. M. & Ng, K. K. *Physics of Semiconductor Devices, Third Edition*. (John Wiley & Sons, Inc., 2006). doi:10.1002/0470068329.

88. Brunin, G., Ricci, F., Ha, V. A., Rignanese, G. M. & Hautier, G. Transparent conducting materials discovery using high-throughput computing. *npj Computational Materials* vol. 5 63 Preprint at https://doi.org/10.1038/s41524-019-0200-5 (2019).

89. Calnan, S. & Tiwari, A. N. High mobility transparent conducting oxides for thin film solar cells. *Thin Solid Films* **518**, 1839–1849 (2010).

90. Kaydanov, V. I., Coutts, T. J. & Young, D. L. Studies of Band Structure and Free-Carrier Scattering in Transparent Conducting Oxides Based on Combined Measurements of Electron Transport Phenomena. in *Materials Research Society Workshop* NREL/CP-520-29064 (Golden, Colorado., 2000). doi:https://digital.library.unt.edu/ark:/67531/metadc719628/m1/1/.

91. Conwell, E. & Weisskopf, V. F. Theory of Impurity Scattering in Semiconductors. *Physical Review* **77**, 388 (1950).

92. Gordon, R. G. Criteria for choosing transparent conductors. *MRS Bull* **25**, 52–57 (2000).

93. Kim, T. *et al.* Megahertz-wave-transmitting conducting polymer electrode for device-to-device integration. *Nat Commun* **10**, 1–11 (2019).

94. Köhnen, E. *et al.* Highly efficient monolithic perovskite silicon tandem solar cells: analyzing the influence of current mismatch on device performance. *Sustain Energy Fuels* **3**, 1995–2005 (2019).

95. Zhang, D., Soppe, W. & Schropp, R. E. I. Design of 4-terminal Solar Modules Combining Thin-film Wide-Bandgap Top Cells and c-Si Bottom Cells. *Energy Procedia* **77**, 500–507 (2015).

96. De Bastiani, M. *et al.* Efficient bifacial monolithic perovskite/silicon tandem solar cells via bandgap engineering. *Nature Energy 2021 6:2* **6**, 167–175 (2021).

97. Rudiger, M., Greulich, J., Richter, A. & Hermle, M. Parameterization of free carrier absorption in highly doped silicon for solar cells. *IEEE Trans Electron Devices* **60**, 2156–2163 (2013).

98. Kim, S. *et al.* Free-carrier absorption and Burstein–Moss shift effect on quantum efficiency in heterojunction silicon solar cells. *Vacuum* **108**, 39–44 (2014).

99. Facchetti, Antonio. & Marks, T. J. Transparent electronics : from synthesis to applications. 448 (2010).

100. Jackson, A. J. *et al.* Computational Prediction and Experimental Realization of Earth-Abundant Transparent Conducting Oxide Ga-Doped ZnSb2O6. *ACS Energy Lett* **2022**, 3807–3816 (2022).

101. Mott, N. F. The transition to the metallic state. *Philosophical Magazine* **6**, 287–309 (1961).

102. Walsh, A., Da Silva, J. L. F. & Wei, S. H. Origins of band-gap renormalization in degenerately doped semiconductors. *Phys Rev B Condens Matter Mater Phys* **78**, 075211 (2008).

103. Maurya, S. K., Galvan, H. R., Gautam, G. & Xu, X. Recent Progress in Transparent Conductive Materials for Photovoltaics. *Energies (Basel)* **15**, 8698 (2022).

104. Hosono, H. Recent progress in transparent oxide semiconductors: Materials and device application. *Thin Solid Films* **515**, 6000–6014 (2007).

105. Zhao, C. *et al.* Burstein-moss effect leads to an unusual suppression of bipolar conduction with shrinking bandgap. *J Mater Chem A Mater* **12**, 23670–23675 (2024).

106. Minami, T. Transparent conducting oxide semiconductors for transparent electrodes. *Semicond Sci Technol* **20**, S35 (2005).

107. Batzill, M. & Diebold, U. The surface and materials science of tin oxide. *Prog Surf Sci* **79**, 47–154 (2005).

108. Özgür, Ü. *et al.* A comprehensive review of ZnO materials and devices. *J Appl Phys* **98**, 041301 (2005).

109. Mryasov, O. N. & Freeman, A. J. Electronic band structure of indium tin oxide and criteria for transparent conducting behavior. *Phys Rev B* **64**, 233111 (2001).

110. De Boer, T., Bekheet, M. F., Gurlo, A., Riedel, R. & Moewes, A. Band gap and electronic structure of cubic, rhombohedral, and orthorhombic In2O3 polymorphs: Experiment and theory. *Phys Rev B* **93**, 155205 (2016).

111. Wang, R. *et al.* Tuning the Surface Electron Accumulation Layer of In2O3 by Adsorption of Molecular Electron Donors and Acceptors. *Small* **19**, 2300730 (2023).

112. Feneberg, M. *et al.* Many-electron effects on the dielectric function of cubic In2O3: Effective electron mass, band nonparabolicity, band gap renormalization, and Burstein-Moss shift. *Phys Rev B* **93**, 045203 (2016).

113. Ganose, A. M. & Scanlon, D. O. Band gap and work function tailoring of SnO2 for improved transparent conducting ability in photovoltaics. *J Mater Chem C Mater* **4**, 1467–1475 (2016).

114. Button, K. J., Fonstad, C. G. & Dreybrodt, W. Determination of the Electron Masses in Stannic Oxide by Submillimeter Cyclotron Resonance. *Phys Rev B* **4**, 4539 (1971).

115. Oshikiri, M., Imanaka, Y., Aryasetiawan, F. & Kido, G. Comparison of the electron effective mass of the n-type ZnO in the wurtzite structure measured by cyclotron resonance and calculated from first principle theory. *Physica B Condens Matter* **298**, 472–476 (2001).

116. Wen, S. J. *et al.* Electrical properties of pure In2O3 and Sn-doped In2O3 single crystals and ceramics. *J Solid State Chem* **101**, 203–210 (1992).

117. Xu, J., Huang, S. & Wang, Z. First principle study on the electronic structure of fluorine-doped SnO2. *Solid State Commun* **149**, 527–531 (2009).

118. Ginley, D. S. & Bright, C. Transparent Conducting Oxides. *MRS Bull* **25**, 15–21 (2000).

119. Ellmer, K. Past achievements and future challenges in the development of optically transparent electrodes. *Nat Photonics* **6**, 809–817 (2012).

120. Koida, T., Fujiwara, H. & Kondo, M. Hydrogen-doped in2O3 as high-mobility transparent conductive oxide. *Japanese Journal of Applied Physics, Part 2: Letters* **46**, L685 (2007).

121. Macco, B. *et al.* Atomic layer deposition of high-mobility hydrogen-doped zinc oxide. *Solar Energy Materials and Solar Cells* **173**, 111–119 (2017).

122. Barraud, L. *et al.* Hydrogen-doped indium oxide/indium tin oxide bilayers for high-efficiency silicon heterojunction solar cells. *Solar Energy Materials and Solar Cells* **115**, 151–156 (2013).

123. Yang, Y. *et al.* CdO as the archetypical transparent conducting oxide. Systematics of dopant ionic radius and electronic structure effects on charge transport and band structure. *J Am Chem Soc* **127**, 8796–8804 (2005).

124. Bright, C. I. *Deposition and Performance Challenges of Transparent Conductive Oxides on Plastic Substrates*. *Transparent Electronics: From Synthesis to Applications* (John Wiley & Sons, Ltd, 2010).

125. Shannon, R. D. Revised effective ionic radii and systematic studies of interatomic distances in halides and chalcogenides. *Acta Crystallographica Section A* **32**, 751–767 (1976).

126. Ágoston, P. Point Defect and Surface Properties of In2O3 and SnO2: A comparative study by first-principles methods. (Technische Universität Darmstadt, 2011).

127. Tang, L. M., Wang, L. L., Wang, D., Liu, J. Z. & Chen, K. Q. Donor-donor binding in In2 O3: Engineering shallow donor levels. *J Appl Phys* **107**, 83704 (2010).

128. Sittinger, V. *et al.* Indium-based transparent conductive oxides developed for perovskite and perovskite-silicon tandem solar cell applications. *Surf Coat Technol* **457**, 129286 (2023).

129. Ying, Z. *et al.* Sputtered Indium-Zinc Oxide for Buffer Layer Free Semitransparent Perovskite Photovoltaic Devices in Perovskite/Silicon 4T-Tandem Solar Cells. *Adv Mater Interfaces* **8**, 2001604 (2021).

130. Ugur, E. *et al.* Enhanced cation interaction in perovskites for efficient tandem solar cells with silicon. *Science* **385**, 533–538 (2024).

131. Zhang, Y. *et al.* High mobility cerium-doped indium oxide thin films prepared by reactive plasma deposition without oxygen. *Vacuum* **206**, 111512 (2022).

132. Morales-Masis, M. *et al.* Highly Conductive and Broadband Transparent Zr-Doped In2O3 as Front Electrode for Solar Cells. *IEEE J Photovolt* **8**, 1202–1207 (2018).

133. Minami, T. Substitution of transparent conducting oxide thin films for indium tin oxide transparent electrode applications. *Thin Solid Films* **516**, 1314–1321 (2008).

134. Seok, H. J. *et al.* ZnO:Ga-graded ITO electrodes to control interface between PCBM and ITO in planar perovskite solar cells. *Sci Technol Adv Mater* **20**, 389–400 (2019).

135. Asvarov, A. S., Abduev, A. K., Akhmedov, A. K. & Kanevsky, V. M. On the Effect of the Co-Introduction of Al and Ga Impurities on the Electrical Performance of Transparent Conductive ZnO-Based Thin Films. *Materials* **15**, 5862 (2022).

136. Akhmedov, A. K., Asvarov, A. S., Muslimov, A. E. & Kanevsky, V. M. Obtaining ZnO-based Transparent Conductive Films with Improved Functional Properties. *Nanobiotechnology Reports* **18**, 865–871 (2023).

137. Chen, X. *et al.* Highly Transparent Conductive Gallium-Doped Zinc Oxide Thin Films Grown by Reactive Plasma Deposition for Silicon Heterojunction Solar Cells. *ACS Appl Electron Mater* **6**, 8488–8496 (2024).

138. Minami, T., Miyata, T. & Tokunaga, H. Electron Scattering from Disordered Grain Boundaries in Degenerate Polycrystalline Al-Doped ZnO Thin Films. *Physica Status Solidi (A) Applications and Materials Science* **216**, 1700783 (2019).

139. Nulhakim, L. & Makino, H. Change of scattering mechanism and annealing out of defects on Ga-doped ZnO films deposited by radio-frequency magnetron sputtering. *J Appl Phys* **119**, 235302 (2016).

140. Sato, Y. & Ikuhara, Y. Role of grain boundaries in ZnO. in *Oxide-based Materials and Devices V* vol. 8987 254–260 (SPIE, 2014).

141. Khan, S. & Stamate, E. Comparative Study of Aluminum-Doped Zinc Oxide, Gallium-Doped Zinc Oxide and Indium-Doped Tin Oxide Thin Films Deposited by Radio Frequency Magnetron Sputtering. *Nanomaterials 2022, Vol. 12, Page 1539* **12**, 1539 (2022).

142. Nomoto, J. ichi *et al.* Comparative study of resistivity characteristics between transparent conducting AZO and GZO thin films for use at high temperatures. *Thin Solid Films* **518**, 2937–2940 (2010).

143. Minami, T., Kuboi, T., Miyata, T. & Ohtani, Y. Stability in a high humidity environment of TCO thin films deposited at low temperatures. *Physica Status Solidi (A) Applications and Materials Science* **205**, 255–260 (2008).

144. Minami, T., Miyata, T., Ohtani, Y. & Kuboi, T. Effect of thickness on the stability of transparent conducting impurity-doped ZnO thin films in a high humidity environment. *physica status solidi (RRL) – Rapid Research Letters* **1**, R31–R33 (2007).

145. Ju, Y. *et al.* The aluminum and titanium-doped zinc oxide films with improved blocking effect on copper diffusion. *Solar Energy* **284**, 112956 (2024).

146. Apergi, S., Brocks, G., Tao, S. & Olthof, S. Probing the Reactivity of ZnO with Perovskite Precursors. *ACS Appl Mater Interfaces* **16**, 14984–14994 (2024).

147. Fullager, D. B., Boreman, G. D., Ellinger, C. D. & Hofmann, T. Broadband optical properties of aluminium zinc oxide thin films prepared by spatial atomic layer deposition. *Thin Solid Films* **653**, 267–273 (2018).

148. Park, H. H. Transparent Electrode Techniques for Semitransparent and Tandem Perovskite Solar Cells. *Electronic Materials Letters* **17**, 18–32 (2021).

149. Ramli, N. F., Aznie Fahsyar, P. N., Ahmad Ludin, N., Yasir, A. S. H. M. & Sepeai, S. Influence of graphene dispersion on the photovoltaic performance of tandem solar cells with four-terminal perovskite–polycrystalline silicon configuration. *Mater Res Express* **11**, 046401 (2024).

150. Lu, S. *et al.* Recent Development in ITO-free Flexible Polymer Solar Cells. *Polymers (Basel)* **10**, 5 (2017).

151. Bardet, L. *et al.* Silver nanowire networks: Ways to enhance their physical properties and stability. *Nanomaterials* **11**, 2785 (2021).

152. Hsu, P. C. *et al.* Performance enhancement of metal nanowire transparent conducting electrodes by mesoscale metal wires. *Nat Commun* **4**, 2522 (2013).

153. Li, Y., Sha, M. & Huang, S. A Review on Transparent Electrodes for Flexible Organic Solar Cells. *Coatings* **14**, 1031 (2024).

154. Zheng, J. *et al.* Monolithic Perovskite-Perovskite-Silicon Triple-Junction Tandem Solar Cell with an Efficiency of over 20%. *ACS Energy Lett* **7**, 3003–3005 (2022).

155. Xu, F. *et al.* Monolithic perovskite/perovskite/silicon triple-junction solar cells with cation double displacement enabled 2.0 eV perovskites. *Joule* **8**, 224–240 (2024).

156. Heydarian, M. *et al.* Monolithic Two-Terminal Perovskite/Perovskite/Silicon Triple-Junction Solar Cells with Open Circuit Voltage >2.8 V. *ACS Energy Lett* **8**, 4186–4192 (2023).

157. Gao, H. *et al.* Thermally Stable All-Perovskite Tandem Solar Cells Fully Using Metal Oxide Charge Transport Layers and Tunnel Junction. *Solar RRL* **5**, 2100814 (2021).

158. Li, Z. *et al.* Semitransparent perovskite solar cells with ultrathin silver electrodes for tandem solar cells. *Solar Energy* **206**, 294–300 (2020).

159. Yang, D. *et al.* 28.3%-efficiency perovskite/silicon tandem solar cell by optimal transparent electrode for high efficient semitransparent top cell. *Nano Energy* **84**, 105934 (2021).

160. Karade, V. C. *et al.* Opportunities and challenges for emerging inorganic chalcogenide–silicon tandem solar cells. *Energy Environ Sci* **18**, 6899–6933 (2025).

161. Sekkat, A. *et al.* Towards enhanced transparent conductive nanocomposites based on metallic nanowire networks coated with metal oxides: a brief review. *J Mater Chem A Mater* **12**, 25600–25621 (2024).

162. Schultheiss, A. *et al.* High performance encapsulation of transparent conductive polymers by spatial atomic layer deposition. *Synth Met* **284**, 116995 (2022).

163. Liang, B. *et al.* Progress in crystalline silicon heterojunction solar cells. *J Mater Chem A Mater* **13**, 2441–2477 (2025).

164. Yang, Q. *et al.* Origin of sputter damage during transparent conductive oxide deposition for semitransparent perovskite solar cells. *J Mater Chem A Mater* **12**, 14816–14827 (2024).

165. Smirnov, Y., Nigmetova, G. & Ng, A. Advances in Top Transparent Electrodes by Physical Vapor Deposition for Buffer Layer-Free Semitransparent Perovskite Solar Cells. *Solar RRL* **8**, 2400354 (2024).

166. Choi, D. *et al.* Carboxyl-functionalized perovskite enables ALD growth of a compact and uniform ion migration barrier. *Joule* **9**, 101801 (2025).

167. Chen, M. *et al.* Atmospheric-pressure atomic layer deposition: recent applications and new emerging applications in high-porosity/3D materials. *Dalton Transactions* **52**, 10254–10277 (2023).

168. Hoye, R. L. Z. *et al.* Spatial Atomic Layer Deposition for Energy and Electronic Devices. *PRX Energy* **4**, 017002 (2025).

169. Macco, B. & Kessels, W. M. M. Atomic layer deposition of conductive and semiconductive oxides. *Appl Phys Rev* **9**, 41313 (2022).

170. Khan, A. *et al.* Stability Enhancement of Silver Nanowire Networks with Conformal ZnO Coatings Deposited by Atmospheric Pressure Spatial Atomic Layer Deposition. *ACS Appl Mater Interfaces* **10**, 19208–19217 (2018).

171. Zhu, Z. *et al.* Low-Temperature Atomic Layer Deposition of Hole Transport Layers for Enhanced Performance and Scalability in Textured Perovskite/Silicon Tandem Solar Cells. *Adv Energy Mater* **14**, 2402365 (2024).

172. Wang, W. C. *et al.* Surface Passivation of Efficient Nanotextured Black Silicon Solar Cells Using Thermal Atomic Layer Deposition. *ACS Appl Mater Interfaces* **5**, 9752–9759 (2013).

173. Ye, H. *et al.* Minimizing the Ohmic Resistance of Wide-Bandgap Perovskite for Semitransparent and Tandem Solar Cells. *Solar RRL* **7**, 2200877 (2023).

174. Zhumagali, S. *et al.* Efficient Narrow Bandgap Pb-Sn Perovskite Solar Cells Through Self-Assembled Hole Transport Layer with Ionic Head. *Adv Energy Mater* **15**, 2404617 (2025).

175. Singh, N., Agarwal, A. & Agarwal, M. Study the effect of band offsets on the performance of lead-free double perovskite solar cell. *Opt Mater (Amst)* **125**, 112112 (2022).

176. Madadi, D. Achieving beyond 26.6% efficiency for graded bandgap perovskite solar cell: Theoretical study. *Mater Chem Phys* **308**, 128231 (2023).

177. Mao, L. *et al.* Fully Textured, Production-Line Compatible Monolithic Perovskite/Silicon Tandem Solar Cells Approaching 29% Efficiency. *Advanced Materials* **34**, 2206193 (2022).

178. Subbiah, A. S. *et al.* Efficient blade-coated perovskite/silicon tandems via interface engineering. *Joule* **9**, 101767 (2025).

179. Werner, J. *et al.* Sputtered rear electrode with broadband transparency for perovskite solar cells. *Solar Energy Materials and Solar Cells* **141**, 407–413 (2015).

180. Castriotta, L. A. *et al.* Semitransparent Perovskite Solar Submodule for 4T Tandem Devices: Industrial Engineering Route Toward Stable Devices. *IEEE J Photovolt* **14**, 433–441 (2024).

181. Bush, K. A. *et al.* 23.6%-efficient monolithic perovskite/silicon tandem solar cells with improved stability. *Nat Energy* **2**, 17009 (2017).

182. Lee, S. W. *et al.* Sputtering of TiO2 for High-Efficiency Perovskite and 23.1% Perovskite/Silicon 4-Terminal Tandem Solar Cells. *ACS Appl Energy Mater* **2**, 6263–6268 (2019).

183. Park, H. H. *et al.* Transparent Electrodes Consisting of a Surface-Treated Buffer Layer Based on Tungsten Oxide for Semitransparent Perovskite Solar Cells and Four-Terminal Tandem Applications. *Small Methods* **4**, 2000074 (2020).

184. Zhu, S. *et al.* Transparent electrode for monolithic perovskite/silicon-heterojunction two-terminal tandem solar cells. *Nano Energy* **45**, 280–286 (2018).

185. Fan, R. *et al.* Toward Full Solution Processed Perovskite/Si Monolithic Tandem Solar Device With PCE Exceeding 20%. *Solar RRL* **1**, 1700149 (2017).

186. Wu, Y. *et al.* Monolithic perovskite/silicon-homojunction tandem solar cell with over 22% efficiency. *Energy Environ Sci* **10**, 2472–2479 (2017).

187. Singha, A. *et al.* Stable and Efficient Large-Area 4T Si/perovskite Tandem Photovoltaics with Sputtered Transparent Contact. *Solar RRL* **7**, 2300117 (2023).

188. Li, C. *et al.* Mitigating VOC Loss in Single-Junction and Four-Terminal Tandem Perovskite/Si Photovoltaics with D-A Phthalocyanines Layers. *Adv Energy Mater* **15**, 2402856 (2025).

189. Fu, F. *et al.* Low-temperature-processed efficient semi-transparent planar perovskite solar cells for bifacial and tandem applications. *Nature Communications 2015* **6**, 8932 (2015).

190. Li, N. *et al.* Room-temperature sputtered aluminum-doped zinc oxide for semitransparent perovskite solar cells. *ACS Appl Energy Mater* **3**, 9610–9617 (2020).

191. Song, H. *et al.* Monolithic perovskite-carrier selective contact silicon tandem solar cells using molybdenum oxide as a hole selective layer. *Energies (Basel)* **14**, 3108 (2021).

192. Hasan, S. A. U., Zahid, M. A., Park, S. & Yi, J. Stability Challenges for a Highly Efficient Perovskite/Silicon Tandem Solar Cell: A Review. *Solar RRL* **8**, 2300967 (2024).

193. Liu, P. *et al.* Interfacial electronic structure at the CH3NH3PbI3/MoOx interface. *Appl Phys Lett* **106**, 193903 (2015).

194. Aydin, E. *et al.* Ligand-bridged charge extraction and enhanced quantum efficiency enable efficient n–i–p perovskite/silicon tandem solar cells. *Energy Environ Sci* **14**, 4377–4390 (2021).

195. Ying, Z. *et al.* Charge-transfer induced multifunctional BCP:Ag complexes for semi-transparent perovskite solar cells with a record fill factor of 80.1%. *J Mater Chem A Mater* **9**, 12009–12018 (2021).

196. Lou, J. *et al.* Designed multi-layer buffer for high-performance semitransparent wide-bandgap perovskite solar cells. *Mater Adv* **4**, 1777–1784 (2023).

197. Ying, Z. *et al.* Hierarchical Micro/Nanostructured Perovskite/Silicon Tandem Solar Cells with Fully Textured Solution-Processed Conformal Perovskite Absorbers. *ACS Energy Lett* **9**, 4018–4023 (2024).

198. Guo, X. *et al.* Oblique-Angle Damage-Free Evaporation of Silicon Oxide Electron-Selective Passivation Contacts for Efficient and Stable Perovskite and Perovskite/TOPCon Tandem Solar Cells. *Adv Energy Mater* **15**, 2403021 (2025).

199. Wang, X. *et al.* Long-chain anionic surfactants enabling stable perovskite/silicon tandems with greatly suppressed stress corrosion. *Nat Commun* **14**, 2166 (2023).

200. Li, B. *et al.* Atomic-Layer-Deposition-Free Monolithic Perovskite/Silicon Tandem Solar Cell Reaching 29.91% Power Conversion on Industrial PERX/TOPCon-like Silicon Bottom Cells. *ACS Energy Lett* **9**, 4550–4556 (2024).

201. Liu, K., Wang, Z., Qu, S. & Ding, L. Stress and Strain in Perovskite/Silicon Tandem Solar Cells. *Nanomicro Lett* **15**, 59 (2023).

202. Zeng, L. *et al.* A Review of Perovskite/Copper Indium Gallium Selenide Tandem Solar Cells. *Solar RRL* **8**, 2301059 (2024).

203. Johnson, S. A. *et al.* Improving the barrier properties of tin oxide in metal halide perovskite solar cells using ozone to enhance nucleation. *Joule* **7**, 2873–2893 (2023).

204. De Bastiani, M. *et al.* Mechanical Reliability of Fullerene/Tin Oxide Interfaces in Monolithic Perovskite/Silicon Tandem Cells. *ACS Energy Lett* **7**, 827–833 (2022).

205. Liu, T. H. *et al.* Bias-free solar to ammonia photoelectrochemical conversion using a perovskite-silicon tandem absorber and 1T-MoS2 integration. *J Mater Chem A Mater* **13**, 12104–12112 (2025).

206. Palmstrom, A. F. *et al.* Enabling Flexible All-Perovskite Tandem Solar Cells. *Joule* **3**, 2193–2204 (2019).

207. Luo, M. *et al.* Novel cathode buffer layer enabling over 21.6%/20.9% efficiency in wide bandgap/inorganic perovskite solar cells. *Nano Energy* **121**, 109162 (2024).

208. Yang, Q. *et al.* Toward the working mechanisms of tin oxide as buffer layer in perovskite/silicon tandem solar cells. *Appl Phys Rev* **12**, 21403 (2025).

209. Jin, Y. *et al.* Efficient and Stable Monolithic Perovskite/Silicon Tandem Solar Cells Enabled by Contact-Resistance-Tunable Indium Tin Oxide Interlayer. *Advanced Materials* **36**, 2404010 (2024).

210. Ramos, F. J. *et al.* Highly efficient MoOx-free semitransparent perovskite cell for 4 T tandem application improving the efficiency of commercially-available Al-BSF silicon. *Sci Rep* **8**, 16139 (2018).

211. Bett, A. J. *et al.* Semi-Transparent Perovskite Solar Cells with ITO Directly Sputtered on Spiro-OMeTAD for Tandem Applications. *ACS Appl Mater Interfaces* **11**, 45796–45804 (2019).

212. Jaysankar, M. *et al.* Four-Terminal Perovskite/Silicon Multijunction Solar Modules. *Adv Energy Mater* **7**, 1602807 (2017).

213. McDonald, C. *et al.* In Situ Grown Nanocrystalline Si Recombination Junction Layers for Efficient Perovskite−Si Monolithic Tandem Solar Cells: Toward a Simpler Multijunction Architecture. *ACS Appl Mater Interfaces* **14**, 33505–33514 (2022).

214. Caudevilla, D. *et al.* Indium tin oxide obtained by high pressure sputtering for emerging selective contacts in photovoltaic cells. *Mater Sci Semicond Process* **137**, 106189 (2022).

215. Liu, Y. *et al.* Equiaxed–columnar stacked TCO films for efficient silicon heterojunction solar cells. *Journal of Materials Science: Materials in Electronics* **33**, 10890–10901 (2022).

216. Akhmedov, A. K., Abduev, A. K., Murliev, E. K., Belyaev, V. V. & Asvarov, A. S. Transparent Conducting Amorphous IZO Thin Films: An Approach to Improve the Transparent Electrode Quality. *Materials* **16**, 3740 (2023).

217. Du, D., Liang, J. & Shen, W. Optimized optical and electrical properties for silicon heterojunction solar cells with an indium tin oxide buffer layer. *Solar Energy Materials and Solar Cells* **286**, 113595 (2025).

218. Seok, H. J., Park, J. M., Lan, S. & Kim, H. K. Sn Composition Engineering Toward the Breakthrough of Transparent Front Electrodes for Efficient and Stable Perovskite Solar Cells. *Adv Energy Mater* **14**, 2301706 (2024).

219. Du, L. *et al.* Indium oxide buffer layer for perovskite/Si 4-terminal tandem solar cells with efficiency exceeding 30%. *Journal of Energy Chemistry* **102**, 189–196 (2025).

220. Hatt, T. *et al.* Electroplated Copper Metal Contacts on Perovskite Solar Cells. *Solar RRL* **5**, 2100381 (2021).

221. Yang, L. *et al.* Study and development of rear-emitter Si heterojunction solar cells and application of direct copper metallization. *Progress in Photovoltaics: Research and Applications* **26**, 385–396 (2018).

222. Brillson, L. J. & Lu, Y. ZnO Schottky barriers and Ohmic contacts. *J Appl Phys* **109**, 121301 (2011).

223. Ye, T. *et al.* Semitransparent Printable Mesoscopic Perovskite Solar Cells for Tandem Solar Cells. *Energy Technology* **10**, 2200524 (2022).

224. Han, W. *et al.* Highly conductive and broadband transparent Zr-doped In2O3 as the front electrode for monolithic perovskite/silicon tandem solar cells. *Progress in Photovoltaics: Research and Applications* **31**, 1032–1041 (2023).

225. Yoon, S. *et al.* Highly Efficient and Reliable Semitransparent Perovskite Solar Cells via Top Electrode Engineering. *Adv Funct Mater* **32**, 2111760 (2022).

226. Magliano, E. *et al.* Solution-Processed Metal-Oxide Nanoparticles to Prevent The Sputtering Damage in Perovskite/Silicon Tandem Solar Cells. *ACS Appl Mater Interfaces* **17**, 17599–17610 (2025).

227. Pingel, S. *et al.* Progress on the reduction of silver consumption in metallization of silicon heterojunction solar cells. *Solar Energy Materials and Solar Cells* **265**, 112620 (2024).

228. Noh, Y. I., Kim, C. U. & Choi, K. J. Perovskite/homojunction-silicon tandem solar cells with optimized silicon nitride passivation and advanced double-sided ohmic contacts. *Mater Today Energy* **52**, 101917 (2025).

229. De Bastiani, M. *et al.* Recombination junctions for efficient monolithic perovskite-based tandem solar cells: physical principles, properties, processing and prospects. *Mater Horiz* **7**, 2791–2809 (2020).

230. Zheng, J. *et al.* Large area efficient interface layer free monolithic perovskite/homo-junction-silicon tandem solar cell with over 20% efficiency. *Energy Environ Sci* **11**, 2432–2443 (2018).

231. Shen, H. *et al.* In situ recombination junction between p-Si and TiO2 enables high-efficiency monolithic perovskite/Si tandem cells. *Sci Adv* **4**, eaau9711 (2018).

232. Li, C. *et al.* Enhancing Efficiency of Industrially-Compatible Monolithic Perovskite/Silicon Tandem Solar Cells with Dually-Mixed Self-Assembled Monolayers. *Adv Funct Mater* **34**, 2407805 (2024).

233. Yao, Y. *et al.* Oriented wide-bandgap perovskites for monolithic silicon-based tandems with over 1000 hours operational stability. *Nat Commun* **16**, 40 (2025).

234. Li, C. *et al.* Deciphering the Impact of Aromatic Linkers in Self-Assembled Monolayers on the Performance of Monolithic Perovskite/Si Tandem Photovoltaic. *Angewandte Chemie - International Edition* **64**, e202420585 (2025).

235. Zhang, X. *et al.* Buried hole-selective interface engineering for high-efficiency tin–lead perovskite solar cells with enhanced interfacial chemical stability. *Sci Bull (Beijing)* **70**, 556–562 (2025).

236. Guo, C. *et al.* Bifacially Reinforced Self-Assembled Monolayer Interfaces for Minimized Recombination Loss and Enhanced Stability in Perovskite/Silicon Tandem Solar Cells. *Advanced Materials* **37**, 2504520 (2025).

237. Xu, D., Wu, P. & Tan, H. Self-assembled monolayers for perovskite solar cells. *Information & Functional Materials* **1**, 2–25 (2024).

238. Puerto Galvis, C. E., González Ruiz, D. A., Martínez-Ferrero, E. & Palomares, E. Challenges in the design and synthesis of self-assembling molecules as selective contacts in perovskite solar cells. *Chem Sci* **15**, 1534–1556 (2024).

239. Li, M., Liu, M., Qi, F., Lin, F. R. & Jen, A. K. Y. Self-Assembled Monolayers for Interfacial Engineering in Solution-Processed Thin-Film Electronic Devices: Design, Fabrication, and Applications. *Chem Rev* **124**, 2138–2204 (2024).

240. Yan, P., Wu, C., Yao, H., Qiu, H. & Hao, F. Self-assembled monolayers for tin perovskite solar cells: challenges and opportunities. *Mater Horiz* **12**, 3188–3200 (2025).

241. Suo, J., Yang, B., Bogachuk, D., Boschloo, G. & Hagfeldt, A. The Dual Use of SAM Molecules for Efficient and Stable Perovskite Solar Cells. *Adv Energy Mater* **15**, 2400205 (2025).

242. Kralj, S. *et al.* Impact of the TCO Microstructure on the Electronic Properties of Carbazole-Based Self-Assembled Monolayers. *ACS Mater Lett* **6**, 366–374 (2024).

243. Leyden, M. R. *et al.* Loading Precursors into Self-Assembling Contacts for Improved Performance and Process Control in Evaporated Perovskite Solar Cells. *Solar RRL* **8**, 2400575 (2024).

244. Huang, Z. *et al.* Highly Efficient Blade-Coated 1.67 eV p-i-n Perovskite Solar Cells Enabled by a Hybrid Self-Assembled Monolayer and Surface Passivation. *ACS Appl Energy Mater* **7**, 11683–11690 (2024).

245. Guo, Y. *et al.* Contact Potential Homogenization via Buried Interface Engineering Enables High-Performance Wide-Bandgap Perovskite Photovoltaics. *Adv Funct Mater* 2500168 (2025).

246. Geng, C. *et al.* Crystallization Modulation and Holistic Passivation Enables Efficient Two-Terminal Perovskite/CuIn(Ga)Se2 Tandem Solar Cells. *Nanomicro Lett* **17**, 1–11 (2025).

247. Zheng, J. *et al.* Polycrystalline silicon tunnelling recombination layers for high-efficiency perovskite/tunnel oxide passivating contact tandem solar cells. *Nat Energy* **8**, 1250–1261 (2023).

248. Zhao, Y. *et al.* Optical Simulation-Aided Design and Engineering of Monolithic Perovskite/Silicon Tandem Solar Cells. *ACS Appl Energy Mater* **6**, 5217–5229 (2023).

249. Zheng, L. *et al.* Inverted perovskite/silicon V-shaped tandem solar cells with 27.6% efficiency via self-assembled monolayer-modified nickel oxide layer. *J Mater Chem A Mater* **10**, 7251–7262 (2022).

250. Phung, N. *et al.* Atomic layer deposition of NiO applied in a monolithic perovskite/PERC tandem cell. *Solar Energy Materials and Solar Cells* **261**, 112498 (2023).

251. Pious, J. K. *et al.* Efficient Blade-Coated Wide-Bandgap Perovskite Solar Cells via Interface Engineering. *ACS Appl Mater Interfaces* **12**, 15 (2025).

252. Wu, M. *et al.* Reconstruction of the Indium Tin Oxide Surface Enhances the Adsorption of High-Density Self-Assembled Monolayer for Perovskite/Silicon Tandem Solar Cells. *Adv Funct Mater* **33**, 2304708 (2023).

253. Er-Raji, O. *et al.* Tuning Self-Assembly of Hole-Selective Monolayers for Reproducible Perovskite/Silicon Tandem Solar Cells. *Small Methods* **9**, 2401758 (2025).

254. Turkay, D. *et al.* Beyond Flat: Undulated Perovskite Solar Cells on Microscale Si Pyramids by Solution Processing. *ACS Energy Lett* **35**, 1397–1403 (2025).

255. Kore, B. P. *et al.* Efficient fully textured perovskite silicon tandems with thermally evaporated hole transporting materials. *Energy Environ Sci* **18**, 354–366 (2025).

256. Messmer, C. *et al.* How to make PERC suitable for perovskite–silicon tandem solar cells: A simulation study. *Progress in Photovoltaics: Research and Applications* **30**, 1023–1037 (2022).

257. Zhao, L., Zhou, C. L., Li, H. L., Diao, H. W. & Wang, W. J. Role of the work function of transparent conductive oxide on the performance of amorphous/crystalline silicon heterojunction solar cells studied by computer simulation. *physica status solidi (a)* **205**, 1215–1221 (2008).

258. Sai, H., Koida, T. & Matsui, T. Improved electrical contact properties in Indium-free silicon heterojunction solar cells with amorphous SnO2 TCO layers. *Solar Energy Materials and Solar Cells* **278**, 113191 (2024).

259. Qiu, D. *et al.* A Review: Application of Doped Hydrogenated Nanocrystalline Silicon Oxide in High Efficiency Solar Cell Devices. *Advanced Science* **11**, 2403728 (2024).

260. Dong, G. *et al.* Power conversion efficiency of 25.26% for silicon heterojunction solar cell with transition metal element doped indium oxide transparent conductive film as front electrode. *Progress in Photovoltaics: Research and Applications* **30**, 1136–1143 (2022).

261. Yu, C. *et al.* Silicon solar cell with undoped tin oxide transparent electrode. *Nat Energy* **8**, 1119–1125 (2023).

262. Yoon, W., Ok, Y. W., Scheiman, D., Rohatgi, A. & Jenkins, P. Impact of Deposition of ITO on Tunnel Oxide Passivating Poly-Si Contact. in *Conference Record of the IEEE Photovoltaic Specialists Conference* 2713–2716 (Institute of Electrical and Electronics Engineers Inc., 2019).

263. Ying, Z. *et al.* Bathocuproine:Ag Complex Functionalized Tunneling Junction for Efficient Monolithic Perovskite/TOPCon Silicon Tandem Solar Cell. *Solar RRL* **6**, 2200793 (2022).

264. Cui, W., Chen, F., Li, Y., Su, X. & Sun, B. Status and perspectives of transparent conductive oxide films for silicon heterojunction solar cells. *Mater Today Nano* **22**, 100329 (2023).

265. Yoon, W. *et al.* Sputtered indium tin oxide as a recombination layer formed on the tunnel oxide/poly-Si passivating contact enabling the potential of efficient monolithic perovskite/Si tandem solar cells. *Solar Energy Materials and Solar Cells* **210**, 110482 (2020).

266. Ding, Z. *et al.* Highly Transparent Oxygen-Doped Poly-Si with In-situ N2O Oxidant for Poly-Si Passivating Contacts in Perovskite/Silicon Tandem Solar Cells. *Solar RRL* **8**, 2400134 (2024).

267. Ding, Z. *et al.* Highly passivated TOPCon bottom cells for perovskite/silicon tandem solar cells. *Nat Commun* **15**, 8453 (2024).

268. Jiang, S. *et al.* Advancing Monolithic Perovskite/TOPCon Tandem Solar Cells by Customizing Industrial-Level Micro-Nano Structures. *Adv Funct Mater* **34**, 2401900 (2024).

269. Hou, Y. *et al.* Efficient tandem solar cells with solution-processed perovskite on textured crystalline silicon. *Science* **367**, 1135–1140 (2020).

270. Isikgor, F. H. *et al.* Concurrent cationic and anionic perovskite defect passivation enables 27.4% perovskite/silicon tandems with suppression of halide segregation. *Joule* **5**, 1566–1586 (2021).

271. Roß, M. *et al.* Co-Evaporated Formamidinium Lead Iodide Based Perovskites with 1000 h Constant Stability for Fully Textured Monolithic Perovskite/Silicon Tandem Solar Cells. *Adv Energy Mater* **11**, 2101460 (2021).

272. Zhumagali, S. *et al.* Linked Nickel Oxide/Perovskite Interface Passivation for High-Performance Textured Monolithic Tandem Solar Cells. *Adv Energy Mater* **11**, 2101662 (2021).

273. Liu, J. *et al.* 28.2%-efficient, outdoor-stable perovskite/silicon tandem solar cell. *Joule* **5**, 3169–3186 (2021).

274. Dabirian, A. *et al.* Metallization of Si heterojunction solar cells by nanosecond laser ablation and Ni-Cu plating. *Solar Energy Materials and Solar Cells* **159**, 243–250 (2017).

275. van de Loo, B. W. H., Macco, B., Melskens, J., Beyer, W. & Kessels, W. M. M. Silicon surface passivation by transparent conductive zinc oxide. *J Appl Phys* **125**, 105305 (2019).

276. Macco, B. *et al.* Temporal and spatial atomic layer deposition of Al-doped zinc oxide as a passivating conductive contact for silicon solar cells. **245**, 111869 (2022).

277. Macco, B. *et al.* Atomic-layer-deposited Al-doped zinc oxide as a passivating conductive contacting layer for n+-doped surfaces in silicon solar cells. *Solar Energy Materials and Solar Cells* **233**, 111386 (2021).

278. Passivating Contacts for Silicon Solar Cells: A Zinc Oxide Breakthrough? – Atomic Limits. https://www.atomiclimits.com/2025/02/04/passivating-contacts-for-silicon-solar-cells-a-zinc-oxide-breakthrough/.

279. Matsui, T. *et al.* Monolithic Perovskite/Silicon Tandem Solar Cells Enabled by Multifunctional TiOx Interconnects. *Small* **21**, 2500969 (2025).

280. Zheng, J. *et al.* Efficient monolithic perovskite–Si tandem solar cells enabled by an ultra-thin indium tin oxide interlayer. *Energy Environ Sci* **16**, 1223–1233 (2023).

281. Nomura, K. *et al.* Room-temperature fabrication of transparent flexible thin-film transistors using amorphous oxide semiconductors. *Nature* **432**, 488–492 (2004).

282. Preissler, N., Bierwagen, O., Ramu, A. T. & Speck, J. S. Electrical transport, electrothermal transport, and effective electron mass in single-crystalline In2O3 films. *Phys Rev B Condens Matter Mater Phys* **88**, 085305 (2013).

283. Koida, T. & Nomoto, J. Effective mass of high-mobility In2O3-based transparent conductive oxides fabricated by solid-phase crystallization. *Phys Rev Mater* **6**, 055401 (2022).

284. Hsu, W. L., Pai, Y. H., Meng, F. S., Liu, C. W. & Lin, G. R. Nanograin crystalline transformation enhanced UV transparency of annealing refined indium tin oxide film. *Appl Phys Lett* **94**, 7 (2009).

285. Mergel, D. & Qiao, Z. Correlation of lattice distortion with optical and electrical properties of In2O3:Sn films. *J Appl Phys* **95**, 5608–5615 (2004).

286. Han, W. *et al.* Light and Carrier Transportation Management in Transparent Electrode for Achieving over 30% Efficiency Perovskite/Silicon Tandem Solar Cells. *ACS Appl Mater Interfaces* **17**, 9297–9304 (2025).

287. Lin, Q., Armin, A., Nagiri, R. C. R., Burn, P. L. & Meredith, P. Electro-optics of perovskite solar cells. *Nat Photonics* **9**, 106–112 (2015).

288. Armin, A. *et al.* Quantum Efficiency of Organic Solar Cells: Electro-Optical Cavity Considerations. *ACS Photonics* **1**, 173–181 (2014).

289. Burkhard, G. F., Hoke, E. T. & McGehee, M. D. Accounting for interference, scattering, and electrode absorption to make accurate internal quantum efficiency measurements in organic and other thin solar cells. *Advanced Materials* **22**, 3293–3297 (2010).

290. Pettersson, L. A. A. *et al.* Modeling photocurrent action spectra of photovoltaic devices based on organic thin films. *J Appl Phys* **86**, 487–496 (1999).

291. Ganesh, V. *et al.* The detailed calculations of optical properties of indium-doped CdO nanostructured films using Kramers-Kronig relations. *J Non Cryst Solids* **552**, 120454 (2021).

292. Bohren, C. F. What did Kramers and Kronig do and how did they do it? *Eur J Phys* **31**, 573 (2010).

293. Shiles, E., Sasaki, T., Inokuti, M. & Smith, D. Y. Self-consistency and sum-rule tests in the Kramers-Kronig analysis of optical data: Applications to aluminum. *Phys Rev B* **22**, 1612 (1980).

294. Vartiainen, E. M. & Peiponen, K.-E. Kramers-Kronig analysis of reflection data. *British Journal of Applied Physics* **16**, 1119 (1965).

295. Jung, H. *et al.* Transparent Electrodes with Enhanced Infrared Transmittance for Semitransparent and Four-Terminal Tandem Perovskite Solar Cells. *ACS Appl Mater Interfaces* **13**, 30497–30503 (2021).

296. Kabaklı, Ö. Ş. *et al.* Thickness Optimization of Front and Recombination ITO in Monolithic Perovskite/Silicon Tandem Solar Cells. *Solar RRL* **8**, 2400454 (2024).

297. Cherif, F. E. & Sammouda, H. Strategies for high performance perovskite/c-Si tandem solar cells: Effects of bandgap engineering, solar concentration and device temperature. *Opt Mater (Amst)* **106**, 109935 (2020).

298. Chime, U. *et al.* Thin silicon heterojunction solar cells in perovskite shadow: Bottom cell prospective. *Solar Energy Materials and Solar Cells* **270**, 112813 (2024).

299. Dewi, H. A. *et al.* Four-Terminal Perovskite on Silicon Tandem Solar Cells Optimal Measurement Schemes. *Energy Technology* **8**, 1901267 (2020).

300. Gharibzadeh, S. *et al.* 2D Surface Passivation in Semi-transparent Perovskite Top Solar Cells with Engineered Bandgap for Tandem Photovoltaics. *Conference Record of the IEEE Photovoltaic Specialists Conference* **2020-June**, 1344–1345 (2020).

301. Kabaklı, Ö. *et al.* Minimizing electro-optical losses of ITO layers for monolithic perovskite silicon tandem solar cells. *Solar Energy Materials and Solar Cells* **254**, 112246 (2023).

302. Heydarian, M. *et al.* Maximizing Current Density in Monolithic Perovskite Silicon Tandem Solar Cells. *Solar RRL* **7**, 2200930 (2023).

303. Li, H. *et al.* Effect of humidity on optical and electrical properties of Zr-doped In2O3 and a new structure for transparent electrode of silicon heterojunction solar cell. *Solar Energy* **196**, 125–131 (2020).

304. Bittkau, K. *et al.* Optical design of spectrally selective interlayers for perovskite/silicon heterojunction tandem solar cells. *Opt Express* **26**, A750–A760 (2018).

305. Li, Y. *et al.* Nanoscale Size Control of Si Pyramid Texture for Perovskite/Si Tandem Solar Cells Enabling Solution-Based Perovskite Top-Cell Fabrication and Improved Si Bottom-Cell Response. *Adv Mater Interfaces* **10**, 2300504 (2023).

306. Chen, B. *et al.* Blade-Coated Perovskites on Textured Silicon for 26%-Efficient Monolithic Perovskite/Silicon Tandem Solar Cells. *Joule* **4**, 850–864 (2020).

307. Artuk, K. *et al.* A Universal Perovskite/C60 Interface Modification via Atomic Layer Deposited Aluminum Oxide for Perovskite Solar Cells and Perovskite–Silicon Tandems. *Advanced Materials* **36**, 2311745 (2024).

308. Qiang, Z. *et al.* A scalable method for fabricating monolithic perovskite/silicon tandem solar cells based on low-cost industrial silicon bottom cells. *Chemical Engineering Journal* **495**, 153422 (2024).

309. Ying, Z. *et al.* Monolithic perovskite/black-silicon tandems based on tunnel oxide passivated contacts. *Joule* **6**, 2644–2661 (2022).

310. Harter, A. *et al.* Perovskite/Silicon Tandem Solar Cells Above 30% Conversion Efficiency on Submicron-Sized Textured Czochralski-Silicon Bottom Cells with Improved Hole-Transport Layers. *ACS Appl Mater Interfaces* **16**, 62817–62826 (2024).

311. Tockhorn, P. *et al.* Nano-optical designs for high-efficiency monolithic perovskite–silicon tandem solar cells. *Nat Nanotechnol* **17**, 1214–1221 (2022).

312. Yang, G. *et al.* Shunt mitigation toward efficient large-area perovskite-silicon tandem solar cells. *Cell Rep Phys Sci* **4**, 101628 (2023).

313. Rehman, A. ur *et al.* Electrode metallization for scaled perovskite/silicon tandem solar cells: Challenges and opportunities. *Progress in Photovoltaics: Research and Applications* **31**, 429–442 (2023).

314. Li, L. *et al.* Buried-Metal-Grid Electrodes for Efficient Parallel-Connected Perovskite Solar Cells. *Advanced Materials* **36**, 2305238 (2024).

315. Jacobs, D. A., Catchpole, K. R., Beck, F. J. & White, T. P. A re-evaluation of transparent conductor requirements for thin-film solar cells. *J Mater Chem A Mater* **4**, 4490–4496 (2016).

316. Messmer, C. *et al.* Optimized front TCO and metal grid electrode for module-integrated perovskite–silicon tandem solar cells. *Progress in Photovoltaics: Research and Applications* **30**, 374–383 (2022).

317. Allen, T. G., Ugur, E., Aydin, E., Subbiah, A. S. & De Wolf, S. A Practical Efficiency Target for Perovskite/Silicon Tandem Solar Cells. *ACS Energy Lett* **10**, 238–245 (2024).

318. Woods-Robinson, R. *et al.* Designing transparent conductors using forbidden optical transitions. *Matter* **6**, 3021–3039 (2023).

319. Kim, H. J. *et al.* High mobility in a stable transparent perovskite oxide. *Applied Physics Express* **5**, 061102 (2012).

320. Cooper, V. R. *et al.* Transparent conducting oxides: A δ-doped superlattice approach. *Sci Rep* **4**, 6021 (2014).

321. Smirnov, Y., Holovsky, J., Rijnders, G. & Morales-Masis, M. Origins of infrared transparency in highly conductive perovskite stannate BaSnO3. *APL Mater* **8**, 61108 (2020).

322. Williamson, B. A. D. *et al.* Resonant Ta Doping for Enhanced Mobility in Transparent Conducting SnO2. *Chemistry of Materials* **32**, 1964–1973 (2020).

323. Zou, Q. *et al.* Tantalum doped tin oxide enabled indium-free silicon heterojunction solar cells with efficiency over 25 %. *Nano Energy* **131**, 110206 (2024).

324. Chen, K. *et al.* Tantalum-doped tin oxide films as an effective diffusion barrier for copper metallization of silicon heterojunction solar cells. *Solar Energy Materials and Solar Cells* **289**, 113681 (2025).

325. Li, K., Willis, J., Kavanagh, S. R. & Scanlon, D. O. Computational Prediction of an Antimony-Based n-Type Transparent Conducting Oxide: F-Doped Sb2O5. *Chemistry of Materials* **36**, 2907–2916 (2024).

326. Boreiko, C. J. & Rossman, T. G. Antimony and its compounds: Health impacts related to pulmonary toxicity, cancer, and genotoxicity. *Toxicol Appl Pharmacol* **403**, 115156 (2020).

327. Mei, Y., Geng, Y., Chen, Z., Xiao, S. & Gao, Z. Ensuring the sustainable supply of semiconductor material: A case of germanium in China. *Int J Prod Econ* **271**, 109231 (2024).

328. Gaisin, R. *et al.* Beryllium intermetallics: Industrial experience on development and manufacture. *Nuclear Materials and Energy* **35**, 101444 (2023).

329. Santos, I. M. *et al.* Next-Generation Solar-Powering: Photonic Strategies for Earth and Space Systems. *Solar RRL* **9**, 2400666 (2025).

330. Kumar, B. K. & Gupta, N. D. Analysis of nanostructured anti reflection coating for various perovskite layer thicknesses in perovskite silicon tandem solar cells. *Mater Res Express* **10**, 126201 (2023).

331. Hu, L. *et al.* Design strategy for p-type transparent conducting oxides. *J Appl Phys* **128**, 140902 (2020).

332. Hautier, G., Miglio, A., Ceder, G., Rignanese, G.-M. & Gonze, X. Identification and design principles of low hole effective mass p-type transparent conducting oxides. *Nat Commun* **4**, 2292 (2013).

333. Singh, J., Bhardwaj, P., Kumar, R. & Verma, V. Progress in Developing Highly Efficient p-type TCOs for Transparent Electronics: A Comprehensive Review. *J Electron Mater* **53**, 7179–7210 (2024).

334. Li, J. *et al.* Enhancing the efficiency and longevity of inverted perovskite solar cells with antimony-doped tin oxides. *Nat Energy* **9**, 308–315 (2024).

335. Sekkat, A. *et al.* Open-air printing of Cu2O thin films with high hole mobility for semitransparent solar harvesters. *Commun Mater* **2**, 1–10 (2021).

336. Sekkat, A. *et al.* Chemical deposition of Cu2O films with ultra-low resistivity: correlation with the defect landscape. *Nat Commun* **13**, 1–11 (2022).

337. Nguyen, V. S. *et al.* Open-air, low-temperature deposition of phase pure Cu2O thin films as efficient hole-transporting layers for silicon heterojunction solar cells. *J Mater Chem A Mater* **9**, 15968–15974 (2021).

338. Woods-Robinson, R. *et al.* P-Type Transparent Cu-Alloyed ZnS Deposited at Room Temperature. *Adv Electron Mater* **2**, 1500396 (2016).

339. Mirza, A. S. *et al.* Cs-Doped and Cs-S Co-Doped CuI p-Type Transparent Semiconductors with Enhanced Conductivity. *Adv Funct Mater* **34**, 2316144 (2024).

340. Mirza, A. S. *et al.* The role of sulfur in sulfur-doped copper(I) iodide p-type transparent conductors. *Matter* **6**, 4306–4320 (2023).

341. Crovetto, A. *et al.* Boron Phosphide Films by Reactive Sputtering: Searching for a P-Type Transparent Conductor. *Adv Mater Interfaces* **9**, 2200031 (2022).

342. Willis, J. *et al.* Prediction and realisation of high mobility and degenerate p-type conductivity in CaCuP thin films. *Chem Sci* **13**, 5872–5883 (2022).